Key Points:
- Groundwater pumping induces ground deformation on multiple spatial and temporal scales
- Different aquifer regions display distinct modes of deformation
- InSAR time series analysis reveals fine scale geologic structures and localized subsidence features

Supporting Information:
- Supporting Information S1

Correspondence to:
B. Riel,
briel@jpl.nasa.gov

Quantifying Ground Deformation in the Los Angeles and Santa Ana Coastal Basins Due to Groundwater Withdrawal

Bryan Riel[1,2] [ID], **Mark Simons[2]** [ID], **Daniel Ponti[3]** [ID], **Piyush Agram[1]**, and **Romain Jolivet[4]** [ID]

[1]Jet Propulsion Laboratory, Pasadena, CA, USA, [2]Seismological Laboratory, California Institute of Technology, Pasadena, CA, USA, [3]United States Geological Survey, Menlo Park, CA, USA, [4]École Normale Supérieure de Paris, Paris, France

Abstract We investigate complex surface deformation within the Los Angeles and Santa Ana Coastal Basins due to groundwater withdrawal and subsequent aquifer compaction/expansion. We analyze an 18 year interferometric synthetic aperture radar (InSAR) time series of 881 interferograms in conjunction with global positioning system (GPS) data within the groundwater basins. The large data set required the development of a distributed time series analysis framework able to automatically decompose both the InSAR and GPS time series into short-term and long-term signals. We find that short-term, seasonal oscillations of ground elevations due to annual groundwater withdrawal and recharge are unsteady due to changes in seasonal withdrawal by major water districts. The spatial pattern of seasonal ground deformation near the center of the basin corresponds to a diffusion process with peak deformation occurring at locations with highest groundwater production. Long-term signals occur over broader areas and are ultimately caused by long-term changes in groundwater production. Comparison of the geodetic data with hydraulic head data from major water districts suggests that different regions of the groundwater system are responsible for different temporal components in the observed ground deformation. Short-term, seasonal ground deformation is caused by compaction of shallower aquifers used for the majority of groundwater production whereas long-term ground deformation is correlated with delayed compaction of deeper aquifers and potential compressible clay layers. These results demonstrate the potential for geodetic analysis to be an important tool for groundwater management to maintain sustainable pumping practices.

1. Introduction

In regions over and adjacent to active aquifer systems, ground deformation can occur as a result of groundwater withdrawal, long-term drought effects, heavy rainfall, and artificial recharge of the aquifers (e.g., Galloway & Burbey, 2011; Todd & Mays, 1980). Ground deformation is a response to changes in pore pressure in the aquifers, which changes the effective stress on the aquifer system's granular matrix and causes contraction or expansion of the pore spaces. From a natural hazard perspective, land subsidence following groundwater withdrawal and compaction of aquifer systems is of particular interest when the subsidence is long term, leading to increased strain on infrastructure, potential formation of earth fissures and surface faults, and changes to surface water drainage (Galloway & Burbey, 2011). Long-term subsidence can occur as a result of a slow decline in groundwater levels or permanent compaction due to effective stress levels exceeding preconsolidation stress levels (Wilson & Gorelick, 1996). More generally, ground deformation due to extraction of fluids in subsurface reservoirs can be described by short-term, elastic responses and long-term, inelastic compression or poroelastic rebound processes (Galloway & Burbey, 2011; Todd & Mays, 1980). Many municipal water districts closely monitor hydraulic head data to track pore pressures in order to maintain sustainable pumping practices and prevent effective stress levels within aquifers from exceeding their preconsolidation levels.

Measurements of ground deformation complement hydraulic head data for groundwater monitoring. Continuous monitoring of ground elevations at discrete points can be achieved through leveling and global positioning system (GPS) data. Additionally, GPS data provides measurements of horizontal motions, which can be useful for quantifying and modeling aquifer properties (Bawden et al., 2001; Galloway & Burbey, 2011). Recently, interferometric synthetic aperture radar (InSAR) has proven to be a very useful remote sensing technique for acquiring spatially dense ground deformation measurements for deformation driven by hydrologic and geothermal fluid processes. Interferograms have been used to observe subsidence in urban

areas due to groundwater withdrawal (Bawden et al., 2001; Buckley et al., 2003), quantify spatial variations of geologic structures in irrigated areas (Valentine et al., 2001), and assess sustainability of groundwater withdrawal and reinjection practices in geothermal plants (Massonnet et al., 1997). From an inverse modeling perspective, the spatial density of ground observations from InSAR data has also allowed for estimation of aquifer system storage parameters (Hoffmann et al., 2003). Studies have shown that InSAR data acquired over sufficient timespans can be used to quantify seasonal deformation caused by the annual cycle of groundwater pumping and recharge, as well as longer-term subsidence from accumulated overdraft of aquifers (Amelung et al., 1999; Bawden et al., 2001; Galloway et al., 1998; Galloway & Hoffmann, 2007). Another class of InSAR techniques uses "stacks" of many coregistered interferograms collected over a finite time period to construct a full time series of ground deformation. These techniques have been used to measure the evolution of land subsidence in the Santa Clara Valley in California (Chaussard et al., 2014; Schmidt & Bürgmann, 2003), subsidence and uplift in Phoenix, Arizona (Miller & Shirzaei, 2015), seasonal uplift and subsidence in the Los Angeles area (Lanari et al., 2004; Watson et al., 2002), etc.

Ground deformation within and around the Los Angeles area has been measured for several decades using GPS data from the Southern California Integrated GPS Network (SCIGN) and InSAR data. Historically, the primary driver for acquiring geodetic data was to quantify the rate of tectonic contraction across the region and the rate of elastic loading on potentially seismogenic faults such as those involved in the 1987 Whittier Narrows and 1994 Northridge earthquakes (e.g., Watson et al., 2002). However, many of the geodetic signals used to study these fault systems are contaminated or completely obscured by nontectonic processes such as groundwater pumping and oil extraction (Bawden et al., 2001). Several geodetic studies have thus aimed to quantify the total contribution of nontectonic sources of deformation for the Los Angeles area.

Bawden et al. (2001) used a series of interferograms from 1997 to 1999 to observe several anthropogenic deformation processes in the basins surrounding the Los Angeles area, including seasonal uplift and subsidence due to groundwater withdrawal in the Santa Ana Coastal Basin which is the primary source of groundwater for Orange County. The larger magnitude of the subsidence signal as compared to the uplift (60 mm for the former, 50 mm for the latter) implied a net subsidence signal in the basin thought to be due to inelastic compaction of lower permeability aquitards within the aquifer system. Watson et al. (2002), Lanari et al. (2004), and Zhang et al. (2012) extended the analysis by Bawden et al. (2001) by including more interferograms over a longer time span. In particular, Lanari et al. (2004) applied the small baseline subset (SBAS) algorithm (Berardino et al., 2002) to produce a time series model from 1995 to 2002. Cross correlation of the spatially varying time series with a reference sinusoid was performed to compute a time shift for each ground point. This time shift map revealed sharp boundaries for the region of the basin responding to the annual groundwater withdrawal and recharging, and heterogeneous time shifts within the basin also suggested lateral variability in hydraulic conductivity. The spatially dense measurements of ground deformation provided by InSAR time series can therefore elucidate subtle characteristics of time-dependent ground deformation within the basin due to changes in aquifer pressure caused by anthropogenic and natural processes. In these studies, seasonal oscillations were generally quantified in an average sense under the assumption that the oscillations were purely sinusoidal with a period of 1 year.

In this study, we first explore the geologic and hydrologic setting of the coastal basins in the Los Angeles area. Following a brief discussion on how groundwater-level changes drive ground deformation in section 2.2, we examine the time history of groundwater levels for the main aquifer systems in section 3.1 using hydraulic head data from the Water Replenishment District (WRD) in Los Angeles and the Orange County Water District (OCWD). We show time series that exhibit highly complex time histories with time-varying seasonal variations and various longer-term trends related to background groundwater levels. We then perform an initial comparison between groundwater levels and surface deformation using GPS data to show that deformation signals with short-term variations are driven by short-term variations in the principal aquifer system while long-term deformation signals appear to be driven by long-term variations in the deeper portions of the aquifer system.

In section 4, we perform an InSAR time series analysis on an expanded data set that includes interferograms from 1992 to 2011 to investigate the spatial variations in short-term, seasonal ground deformation. By using the assumption that seasonal ground motions can be represented by a linear combination of sinusoids, we can compare the timing and amplitude of peak seasonal deformation of ground points within the basin to study the effects of aquifer geometry, groundwater pumping practices, and hydraulic conductivity on the

ground response. This method of time series analysis is similar to the ones used in Bawden et al. (2001) and Watson et al. (2002). However, since both hydraulic head and ground deformation time series show nonsinusoidal seasonal variations, in section 5, we develop a new method for InSAR time series analysis that automatically decomposes the time series into generic long-term and short-term signals. We compare the decomposed InSAR time series to all available monitoring wells to better understand the relationship between deformation signals of different durations and different regions of the groundwater system. Finally, in section 6, we discuss how these results are related to groundwater management with regards to sustainable pumping practices and we relate several of our InSAR observations to physical processes based on groundwater dynamics.

2. Background

2.1. Hydrogeology and Structure of the Los Angeles Basins

The Los Angeles area consists of several basins containing groundwater systems, including the Los Angeles Central and West Coast Basins and the Santa Ana Coastal Basin in Orange County (Figure 1). The Central and West Coast Basins lie within Los Angeles County and are monitored by WRD whereas the Santa Ana Coastal Basin lies within Orange County and is monitored by OCWD. The Los Angeles Central Basin (hereafter referred to as the Central Basin) is separated from the West Coast Basin by the northern portion of the Newport-Inglewood Fault Zone (NIF), which acts locally as a barrier for fluid flow between the two basins (Thiros et al., 2010). In this study, we focus on ground deformation within the Central and Santa Ana Coastal Basins. While this region is tectonically active (about 4 mm/yr of uniaxial contraction along thrust faults; Bawden et al., 2001), motion along the major faults bounding the basins is relatively minimal compared to the seasonal motion caused by groundwater fluctuations (less than 1 mm/yr for NIF; Southern California Earthquake Data Center, 2012).

Both the Central and Santa Ana Coastal Basins have groundwater systems with similar structural characteristics. The forebay area occupies about 38 percent of the Santa Ana Coastal Basin and occupies the eastern region that meets the Santa Ana Mountains (Figure 1). Here unconfined vertical movement of water is not restricted by laterally extensive clay layers (Woodside & Westropp, 2015). Groundwater recharge occurs mainly in the forebay area. The confined area (also known as the "pressure area") is considerably larger and extends from the western edge of the forebay area to the Pacific Ocean (Thiros et al., 2010). Here there are laterally continuous thick layers of silt and clay that restrict vertical flow of groundwater, causing aquifers to be under confining pressure. While the actual groundwater system consists of several contiguous aquifer units, clay interbeds, and confining aquitards, the OCWD has developed a simplified model consisting of shallow, middle (principal), and deep aquifer systems to approximate groundwater flow (Figure 2; Ehman et al., 2014; Woodside & Westropp, 2015). The shallow aquifer system generally spans depths of up to 60 m for most of the basin and is unconfined in the forebay region. The principal aquifer system, which supports over 90% of the basin pumping in Orange Country, is generally greater than 300 m thick for much of the basin. The deep aquifer system, which is limited in production capability due to the presence of amber colored groundwater (which requires extra treatment to remove colors and odors from the water), defines water-storing units up to 600 m in depth in the center of the Santa Ana Coastal Basin (Woodside & Westropp, 2015).
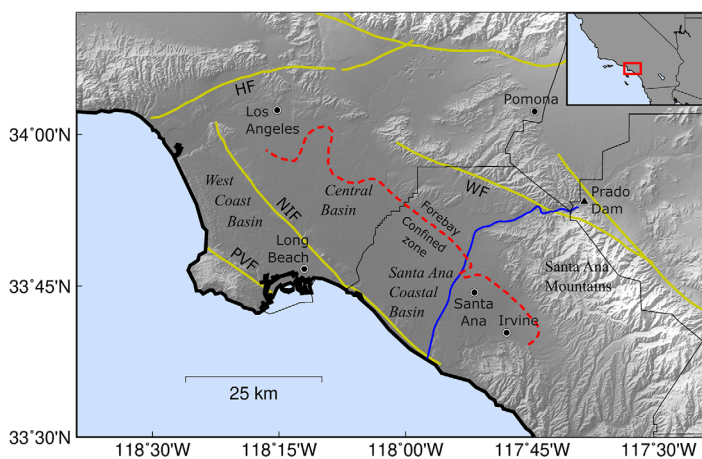

Figure 1. Location and tectonic setting of the Los Angeles Central and West Coast Basins and the Santa Ana Coastal Basin. The thick gold lines represent major faults in the area, including the Newport-Inglewood Fault (NIF), the Whittier Fault (WF), the Palos Verdes Fault (PVF), and the Hollywood Fault (HF). The thin black lines indicate county boundaries, and the thick blue line corresponds to the Santa Ana River. The Prado Dam on the east side of the Santa Ana Mountains is the primary flood control facility for the downstream Santa Ana River. The dashed red line indicates the approximate boundary between the forebay and confined areas of the groundwater system modified from estimates by the WRD and OCWD. The inset shows the location of the study area along the California coast.

2.2. Aquifer Compaction Theory

The relationship between ground deformation and aquifer pressure for *confined* aquifers can be explained using groundwater flow theory based on the Principle of Effective Stress (Terzaghi, 1923). Effective stress can be expressed as
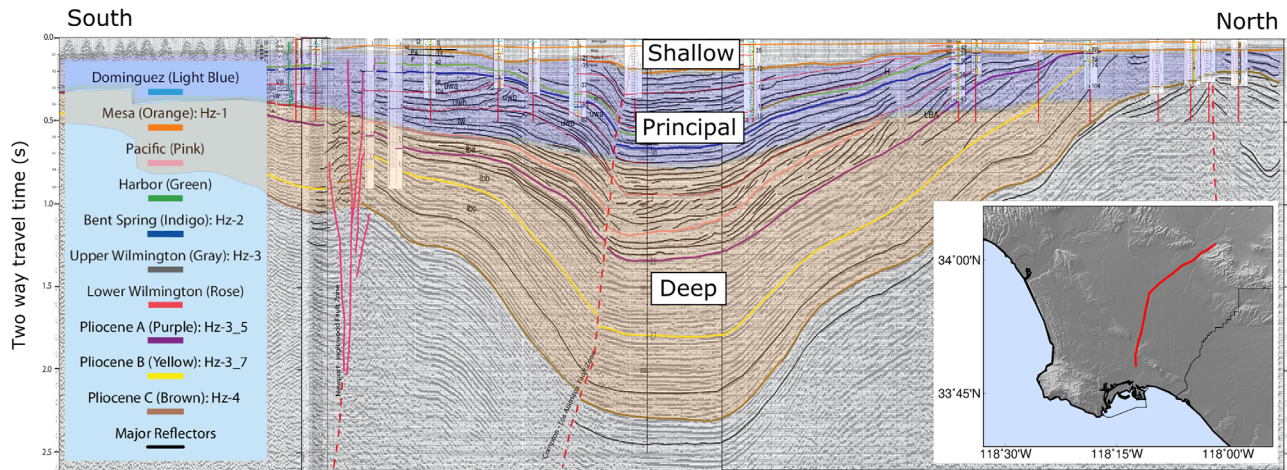
Figure 2. Stratigraphic framework of the Los Angeles Basin (modified from Sheet 19 in Ehman et al., 2014). Aquifer structure is interpreted from connected seismic lines within the basin (red line in map inset). Boundaries of stratigraphic sequences are indicated by solid colored lines, and the locations and depths of several United States Geological Survey (USGS) monitoring wells projected onto the seismic line are also shown. The purple shaded area indicates the approximate depth extent of the "principal" aquifer system, i.e., the depth range where most groundwater withdrawal occurs. The orange shaded area indicates the deep aquifer system while the unshaded sequences are associated with the shallow aquifer system. One second in two-way travel time is approximately equal to 1.1 km.

$$\sigma'_{ij} = \sigma_{ij} - \delta_{ij} p, \tag{1}$$

where σ'_{ij} and σ_{ij} are components of the effective and total stress tensors, respectively, p is the pore fluid pressure, and δ_{ij} is the Kronecker delta where $\delta_{ij} = \begin{cases} 1, \text{if } i=j \\ 0, \text{if } i \neq j \end{cases}$. Assuming a Newtonian fluid and strains primarily for the zz component (due to the natural horizontal orientation of aquifer units), we can simplify equation (1) to

$$\sigma'_{zz} = \sigma_{zz} - p. \tag{2}$$

By also assuming that changes in the total/overburden stress are negligible for our study period (since hydraulic head changes do not change the state of the confining units), changes in effective stress can then be simply expressed as

$$\Delta \sigma'_{zz} = -\Delta p. \tag{3}$$

Note that the assumption of constant overburden stress does not apply to unconfined aquifers since by definition they are not under confining stress. It can be shown that changes in stress can be related to changes in hydraulic head as (Heath, 1982)

$$\Delta \sigma'_{zz} = -\rho_w g \Delta h, \tag{4}$$

where h is the hydraulic head, ρ_w is the density of water, and g is the gravitational acceleration constant. In order to relate pore fluid pressure changes to ground deformation, we use the definition for one-dimensional skeletal compressibility, α, as the ratio of vertical strain to vertical effective stress:

$$\alpha = \frac{-\Delta b / b}{\Delta \sigma'_{zz}}, \tag{5}$$

where the Δb is the change in thickness of a control volume with initial thickness b (Galloway & Burbey, 2011). This equation thus relates the compaction and expansion of sediments to changes in effective stress; integrated compaction over the entire depth of the aquifer system is equivalent to what we measure as land subsidence (Chen et al., 2016). The skeletal specific storage, $S_{S_k} = \rho_w g \alpha$, can be used to combine equations (4) and (5) as

$$S_{S_k} b = S_k = \frac{\Delta b}{\Delta h}, \tag{6}$$

where S_k is the skeletal storage coefficient. The storage coefficient (storativity), S, is the sum of S_k and a component of the aquifer system storage attributed to the compressibility of water; therefore, when water is assumed to be incompressible, $S = S_k$. This same relationship holds for the specific storage, S_s, and the skeletal specific storage, S_{S_k}. In unconfined aquifers, the storativity is also controlled by the specific yield, S_y, such that $S = S_y + S_{S_k} b$. However, in unconfined aquifers, the contribution from the specific yield is usually much larger than that due to compression of the aquifer.

Consolidation experiments on typical sediments have shown that specific storage for a given material can behave very differently depending on whether the effective stress is above or below the preconsolidation stress (i.e., the previous maximum effective stress). This boundary essentially separates the regimes of elastic and inelastic deformation depending on the head level. To account for these two regimes, two separate skeletal specific storages are used:

$$S_{S_k} = \begin{cases} S_{S_{ke}} & \text{for } \sigma'_{zz} < \sigma'_{zz(pre)} \\ S_{S_{kv}} & \text{for } \sigma'_{zz} \geq \sigma'_{zz(pre)}, \end{cases} \tag{7}$$

where $S_{S_{ke}}$ and $S_{S_{kv}}$ are the elastic and inelastic skeletal specific storage coefficients, respectively. In the inelastic regime when head drops below the preconsolidation level (the previous level of minimum hydraulic head), irreversible loss of water storage occurs, and in the case where this state persists, the skeletal specific storage is expected to vary proportionally to the logarithm of the effective stress (Galloway & Burbey, 2011). From a water management perspective, the preconsolidation level is used to define sustainable pumping rates in order for aquifer deformation to remain elastic.

## 3. Groundwater Level and Ground Deformation Time History

3.1. Monitoring Groundwater Levels With Hydraulic Head Time Series

Since the primary driver of ground deformation within the coastal basins is changes in aquifer pressure (section 2.2), we gather data from several multiport monitoring wells located within the coastal basins that measure hydraulic head levels at various aquifer depths. Here we use twelve monitoring wells operated by WRD and thirty wells operated by OCWD (Figure 3). For both sets of wells, the depths of the sample ports allow us to determine hydraulic head levels for distinct aquifer units. For unconfined aquifers, the hydraulic head is the elevation of the water table where the hydrostatic pressure of the water is equal to the atmospheric pressure. For confined aquifers, the hydraulic head level corresponds to the piezometric (or potentiometric) surface, which is the elevation water would rise to in a piezometric well (Todd & Mays, 1980). Groundwater levels as measured by hydraulic head time series for OCWD well station SAR-9 (located in the middle of the Santa Ana Coastal Basin encompassing the confined aquifers) show large annual oscillations, particularly at the depth of the principal aquifer system (Figure 4). These oscillations are caused by the annual cycle of groundwater recharge (artificial and natural) and withdrawal. From the early 1990s to the mid-2000s, groundwater levels typically peaked around March after the rainy season and are at their lowest toward the end of the summer during the heaviest periods of groundwater withdrawal. This time period also corresponds to the largest annual fluctuations in groundwater levels due to water storage programs that encouraged increased groundwater withdrawal during the summer months when regional demand for imported water is higher (Woodside & Westropp, 2015). Superimposed over the annual water-level fluctuations are longer-term variations. Generally, we can observe a decrease in overall water levels, which started in 1970 after the basin was essentially refilled after replenishment from Colorado River water (Woodside & Westropp, 2015). We can also observe two transient increases in groundwater levels in 2005 and in 2012, both of which followed periods of decreased pumping activity due to increased water flow (base flow from the upstream watershed plus storm runoff) into the Santa
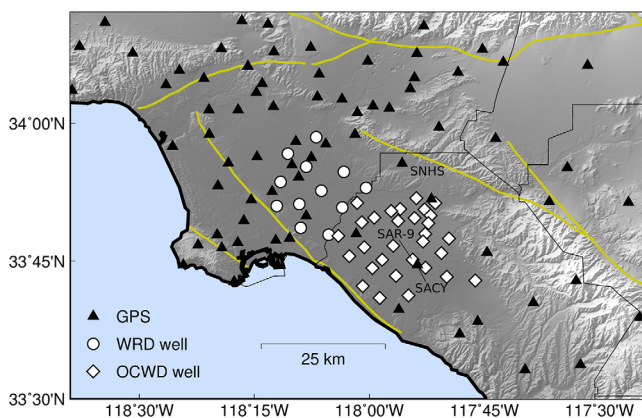
Figure 3. Distribution of continuous GPS and well data used in this study. The white circles correspond to WRD wells used in this study while the white diamonds correspond to OCWD wells. The black triangles show the GPS coverage in this area. Hydraulic head time series for OCWD well station SAR-9 is shown in Figure 4. GPS data were acquired from the Scripps Orbit and Permanent Array Center (SOPAC; http://sopac.ucsd.edu/). All GPS data used in this study have been postprocessed for outlier removal and common mode filtering.
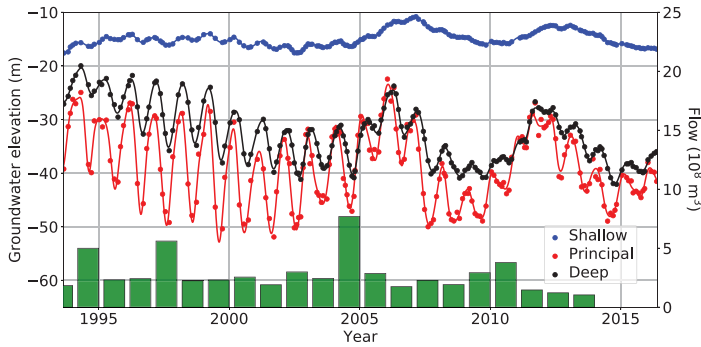
Figure 4. Hydraulic head time series for OCWD well SAR-9 for selected ports in the shallow, principal, and deep aquifer systems. The dots represent the raw head data while the solid lines are interpolated data using smoothing splines. The green bars represent the total water flow into the Santa Ana River (base plus storm flow) measured at Prado Dam (Woodside & Westropp, 2015). The largest head variations occur in the principal aquifer system, where the majority of groundwater withdrawal occurs.

Ana River. Note that during other periods of increased water flow into the Santa Ana River (e.g., around 1995 and 1998), groundwater levels did not see a corresponding increase because groundwater production was not adjusted in response to the increased inflow (see section 6.1 for further discussion).

3.2. Groundwater Diffusion and Varying Response Times

Since groundwater is pumped at discrete points within the Central and Santa Ana Coastal Basins, we expect spatial variations in hydraulic head changes in response to pressure gradients. Low permeabilities in clay interbeds and confining units can cause time delays in hydraulic head levels from one aquifer unit to another, as well as intraaquifer delays. Additionally, variations in aquifer thickness can affect the propagation of hydraulic head changes.

Three-dimensional flow of ground water in porous media can be described by the differential equation for a control volume (e.g., Jacob, 1950; Keranen et al., 2014):

$$\frac{\partial v_x}{\partial x} + \frac{\partial v_y}{\partial y} + \frac{\partial v_z}{\partial z} = -S_s \frac{\partial h}{\partial t} + Q(t,x,y,z), \tag{8}$$

where v_x, v_y, and v_z are the rectangular components of the instantaneous bulk fluid velocity in the control volume, and $Q(t,x,y,z)$ is a source term that can vary in time and in space. For the purpose of this discussion, we assume one-dimensional flow in the x-direction. From equation (8), it can be shown that propagation of hydraulic head in an aquifer can be written as (Hantush, 1962)

$$K\frac{\partial b}{\partial x}\frac{\partial h}{\partial x} + b\frac{\partial K}{\partial x}\frac{\partial h}{\partial x} + bK\frac{\partial^2 h}{\partial x^2} = S_s b \frac{\partial h}{\partial t} - Q(t,x), \tag{9}$$

where $K=K(x)$ is the hydraulic conductivity and $b=b(x)$ is the aquifer thickness. In the special case of flow through an aquifer with uniform thickness and conductivity, equation (9) can be written as (Fetter, 2000)

$$K\frac{\partial^2 h}{\partial x^2} = S_s \frac{\partial h}{\partial t} - Q(t,x). \tag{10}$$

For the following discussion, let us assume a point source, $Q(t,x)=Q(t)\delta(x-x_0)$, and assume $Q(t)$ is periodic to represent groundwater recharge and withdrawal. Therefore, for a time-varying source with a temporal frequency ω, $Q(t)=\cos \omega t$, the solution to equation (10) will have the approximate form (Guenther & Lee, 1996):

$$h(x,t) \approx e^{-\sqrt{2\omega}|x-x_0|}\cos\left(\sqrt{2\omega}|x-x_0|\pm\omega t\right). \tag{11}$$

In the above equation, there is a frequency dependent attenuation term that would damp out the diffusion of the hydraulic head at higher source frequencies. In other words, head variations due to a point source perturbation in water pressure (such as a production well) would decay more rapidly away from the source for a faster withdrawal/pumping cycle. The ωt factor in the periodic term in the above equation controls the rate of diffusion, or hydraulic response time, of the pressure perturbation. For larger ω, we would expect a shorter response time. By solving for the homogeneous solution to equation (10), we can also estimate the material-dependent response time for confined aquifers as (Alley et al., 2002)

$$T^* = S_s L_c^2 / K, \tag{12}$$

where T^* is the response time and L_c is a characteristic thickness for a specific aquifer unit. By defining the hydraulic diffusivity as the ratio K/S_s, it can be seen that aquifers with a higher diffusivity would experience shorter response times.

To assess timing differences in the vertical dimension, we use the SAR-9 hydraulic head data to estimate the amplitude and time to peak signal for the annual oscillations in head. Since the head data contain both seasonal variations and long-term trends, we model the time series as a linear combination of sinusoids

with annual and semiannual periods for the seasonal signal and third-order integrated B-splines (hereafter referred to as B^i-splines; see Hetland et al., 2012) for the transient, long-term trends:

$$h(t) = \sum_{i=1}^{2}\left[a_i\cos\frac{2\pi}{T_i}t + b_i\sin\frac{2\pi}{T_i}t\right]$$
$$+ \sum_{j=1}^{32} c_j B^i\left(t - t_j\right), \tag{13}$$

where $T_1 = 0.5$ years and $T_2 = 1$ year, and $B^i(t - t_j)$ represent the B^i-splines centered at time t_j (Hetland et al., 2012). Here we partition the data time span into 32 evenly spaced knot times t_j so that the B^i-splines each have an effective duration of $2 * (t_j - t_{j-1})$. We estimate the coefficients a_i, b_i, and c_j simultaneously using regularized least squares for the cost function:

$$J(\mathbf{m}) = \operatorname*{argmin}_{\mathbf{m}} ||\mathbf{h} - \mathbf{Gm}||_2^2 + \mathbf{m}^T \mathbf{C_m}^{-1}\mathbf{m}, \tag{14}$$

where $\mathbf{h}$ is the time series data, $\mathbf{G}$ is the temporal design matrix containing the sinusoids and B^i-splines along the columns, $\mathbf{m}$ is the vector of coefficients of the elements in $\mathbf{G}$, and $\mathbf{C_m}$ is a prior covariance matrix for regularization. For this analysis, we set $\mathbf{C_m}$ to be the identity matrix with an optimal scaling coefficient selected using k-fold cross validation. After estimating $\mathbf{m}$ for each well, we can compute the amplitude and phase delay for each seasonal component as

$$A_i = \sqrt{a_i^2 + b_i^2}, \tag{15}$$

$$\phi_i = \tan^{-1}\left(\frac{b_i}{a_i}\right), \tag{16}$$

where A_i is the amplitude and ϕ_i is the phase delay, or time to peak signal. We repeat this procedure for the time series at each port depth to estimate the time to reach peak head levels for the seasonal signal between 1996 and 2006 (supporting information Table S2.1) and for the transient increase starting in 2004–2005
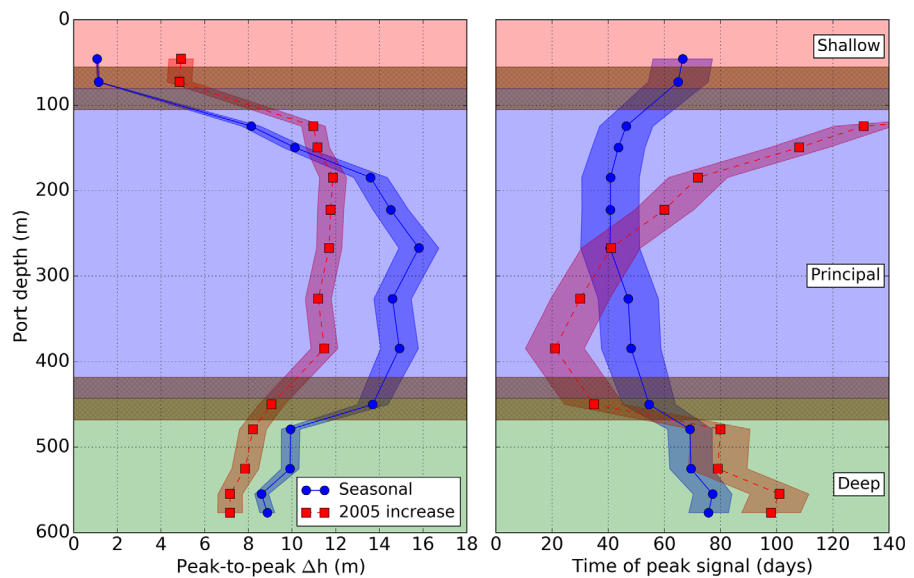
Figure 5. Depth profile of (left) amplitude and (right) phase delay of SAR-9 hydraulic head data. The blue lines correspond to the average seasonal oscillations while the red lines correspond to the water-level recovery signal initiating in 2004/2005 due to decreased pumping activity. The horizontal shaded areas centered on the blue and red lines indicate the uncertainties associated with those values. The vertical shaded areas represent the depths corresponding to the three aquifer system layers as estimated by the OCWD three-layer model, and the brown hatched regions indicate the approximate range of depths of the aquitards separating the aquifer system layers. The amplitudes for both the seasonal oscillation and transient increase are largest in (left) the principal zone; correspondingly, the phase delays are shorter in (right) the principal zone.

caused by a decrease in overall groundwater withdrawal (Figure 5). For both the annual and transient peak signals, we observe that water levels in the principal aquifer system reach peak levels earlier than both the shallow and deep aquifer systems. The peak-to-peak seasonal increases in water levels are much higher in the principal aquifer system, which is expected since 90% of groundwater withdrawal is from the confined principal aquifer system.

The depth-dependent timing for the annual signal and 2004–2005 transient signal are noticeably different. It appears to take longer for hydraulic head levels to equilibrate for the 2005 increase than for the annual cycle. These observations are consistent with the solution to 1-D diffusion in equation (11). The transient increase in groundwater levels following 2005 has an effective period of ~4 years while the seasonal cycle of recharge and withdrawal has a period of ~1 year. The former has a slower rate of diffusion but lower attenuation of head amplitudes within the aquifer system whereas the latter has a higher diffusion speed but much more rapid attenuation of amplitude with depth. We conclude that the timing differences between these two processes are entirely due to variations in the temporal character of the source.

Propagation of hydraulic head is described by a three-dimensional diffusion process. We thus investigate timing differences in the horizontal direction by estimating the average time of peak hydraulic head for all wells in the principal aquifer system using the same modeling procedure in equation (13). Because the OCWD model for the depths of the shallow, principal, and deep aquifer systems is only an approximation of the actual basin structure, we classify monitoring wells as being located within the "principal" aquifer system primarily by the characteristics of their hydraulic head time series. Specifically, for each well, we choose ports with the largest seasonal variations in head levels (typically more than 2 times the variations of the shallowest ports) and with similar times of peak hydraulic head (1–2 months differences in peak head times) since diffusion should be relatively fast in the principal aquifer system. We then compute the median peak time of those ports to represent the peak time for that well.

Monitoring wells in the center of the basin have earlier peak times than wells in the margins of the basin (Figure 6). The principal aquifer system generally reaches peak groundwater levels between February and March in the central region of the basin while the margins peak between March and April. Since the principal aquifer system is thickest and most productive in the center of the basin, the majority of groundwater production is obtained from units in the basin center. Thus, the earlier peak times for the central monitoring wells are mostly controlled by the timing of nearby pumping activity. Within about 10–15 km from the basin center, and particularly in the Santa Ana Coastal Basin, we can observe a gradient in peak times from
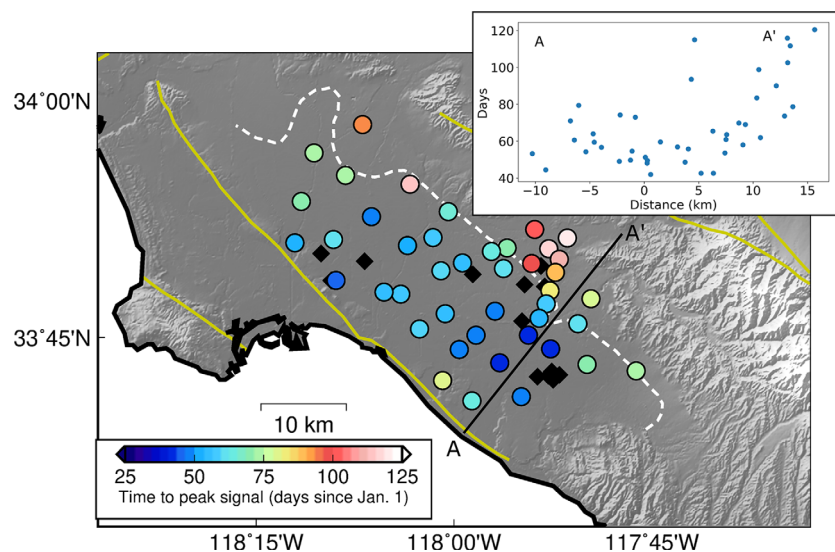
Figure 6. Time to peak seasonal signal for hydraulic head data from well ports located in the principal aquifer system. Large-scale production wells (wells with seasonal withdrawal volume amplitudes greater than 3.7×10^5 m^3 [300 ac ft]) are indicated by black diamonds. Wells in the center of the basin closer to areas of concentrated pumping reach their peak signals earlier in the year compared to wells in the margins of the basin. Inset shows timing of wells projected onto the A–A' line. The dashed white line indicates the approximate boundary between the forebay and confined areas.

the center toward the margins, which suggests horizontal propagation of pressure away from the main pumping sites. Comparison of the propagation speeds of groundwater in the vertical and horizontal directions in the center of the basin for the annual cycle reveals that propagation speeds are approximately 1 order of magnitude slower in the vertical direction than the horizontal direction (∼30 m/d versus ∼300 m/d, respectively). This discrepancy is consistent with the general observation that vertical conductivity is much lower than horizontal conductivity due to the horizontal orientation of bedding and the likely presence of laterally continuous clay beds within the main aquifer units that impede vertical groundwater flow. This propagation signal becomes a little less clear in the Central Basin in Los Angeles County, which is likely affected by the existence of a shelf that extends east from the NIF limiting the interconnectivity of aquifer units.

The later peak times in the eastern margin of the basin (closer to the recharge zone) are later than expected for normal horizontal diffusion. Groundwater flow in this area is substantially different than in the center of the basin due to the unconfined and semiconfined nature of aquifer units that are pumped in this area. Due to the bowl-shaped structure of the basin and the overall thinning of aquifers from the center of the basin toward the margins, groundwater withdrawal in the center of the basin occurs primarily from *younger*, shallower units while withdrawal in the margins occurs primarily from *older*, deeper units that are likely folded and deformed (see Figure 2). These stratigraphic differences will also be associated with large variations in storage coefficient between confined and unconfined aquifer units. Therefore, the later delay times for the wells in the eastern margin may be due to the effect of greater vertical propagation of groundwater from older units to younger units and large lateral variations in storage coefficient. Other factors could include lateral variations in hydraulic conductivity or the presence of faults acting as barriers to fluid flow.

3.3. Ground Deformation History

From equation (6), we know that ground deformation over a confined aquifer is approximately proportional to changes in hydraulic head under certain simplifying assumptions, mainly that aquifer or aquitard compression and expansion is elastic for effective stress levels less than the previous maximum effective stress. The proportionality constant in the elastic relationship is the skeletal storage coefficient, S_k. However, ground deformation can also be affected by inelastic compaction of clays in aquitards and clay-rich interbeds. In this case, ground deformation will not be correlated with hydraulic head and is expected to vary exponentially with time (Chaussard et al., 2014). The exponential relationship is derived from the theory of hydrodynamic consolidation and is used to describe the delayed response of fine-grained materials after effective stress levels have surpassed previous maximum levels.

We start with the hypothesis that all deformation within the basin is elastic. For short-term signals driven by the annual cycle of groundwater withdrawal and recharge, this assumption is most likely to be true since groundwater levels over the past two decades have been consistently higher than levels in the first half of the twentieth century (Woodside & Westropp, 2015). Additionally, the common driving mechanism for inelastic deformation associated with compressible materials typically occurs over a long time span, although rapid, substantial stress increases can also lead to rapid inelastic deformation. In order to test the hypothesis of purely elastic deformation, we must compare short-term deformation signals with short-term variations in hydraulic head and long-term deformation signals with long-term variations in hydraulic head. As discussed in section 1, the observed deformation on the ground surface is a result of the integrated compaction of aquifers and aquitards along the entire depth of the aquifer system. However, we also know that there is a time delay for a pressure perturbation to diffuse throughout an aquifer system (e.g., Figure 5). This time delay is dependent on hydraulic diffusivity along the diffusion path and the rate of pressure change at the pressure source (e.g., groundwater withdrawal rate). Therefore, different regions of the aquifer systems will be compacting/expanding at different times. By comparing ground deformation time series with hydraulic head time series at various depths, we can estimate the effective depth at which aquifer deformation is most correlated with ground deformation. In the ideal case, this depth would approximate the depth of a hypothetical localized pressure source.

We examine vertical displacement data from the GPS station SACY, which is part of SCIGN and is located about 1.4 km away from the SAR-9 well (Figure 3). We decompose both the GPS vertical displacements and the SAR-9 head time series into long-term and short-term (seasonal) signals using a modified form of equation (13). Instead of using sinusoids to model the seasonal signals, we use a linear combination of third-

order B-splines (different than the integrated B-splines used for transient signals) to allow for seasonal signals with time-varying amplitudes and phase delays. We assign the temporal support of the B-splines such that the seasonal signal each year is described by a linear combination of B-splines spaced 0.2 years apart. With this approach, we could reconstruct seasonal signals with wide variations from year to year. In this study, we construct $\mathbf{C_m}$ in equation (14) such that B^i-splines are independent while B-splines are correlated with other B-splines that share the same centroid time within any given year (e.g., B-splines centered in March are correlated with other B-splines centered in March). We assign the correlation strength for the B-splines to be exponentially decaying in time with a decay time of two years. The decay time was experimentally chosen in order to maintain the flexibility of the B-splines to model time-varying seasonal signals while still enforcing a level of coherency from year to year.

After decomposing the SACY vertical displacements and the SAR-9 hydraulic head time series at multiple port depths into long-term and short-term components, we compute the Pearson correlation coefficients between each head time series and the GPS time series. We fit the correlation coefficient depth profiles with third-order polynomials in order to reduce the noise of the coefficient estimation and estimate the depth of maximum correlation between hydraulic head and ground deformation. We then compute an optimal scaling factor between the GPS and head time series at the depth of maximum correlation (analogous to S_k in equation (6)).

For both the long-term and short-term components, the vertical ground displacement data is well matched by hydraulic head variations at a given depth (Figure 7). The transition from regular groundwater fluctuations (caused by the annual cycle of recharge and withdrawal) to unsteady oscillations between 2008 and
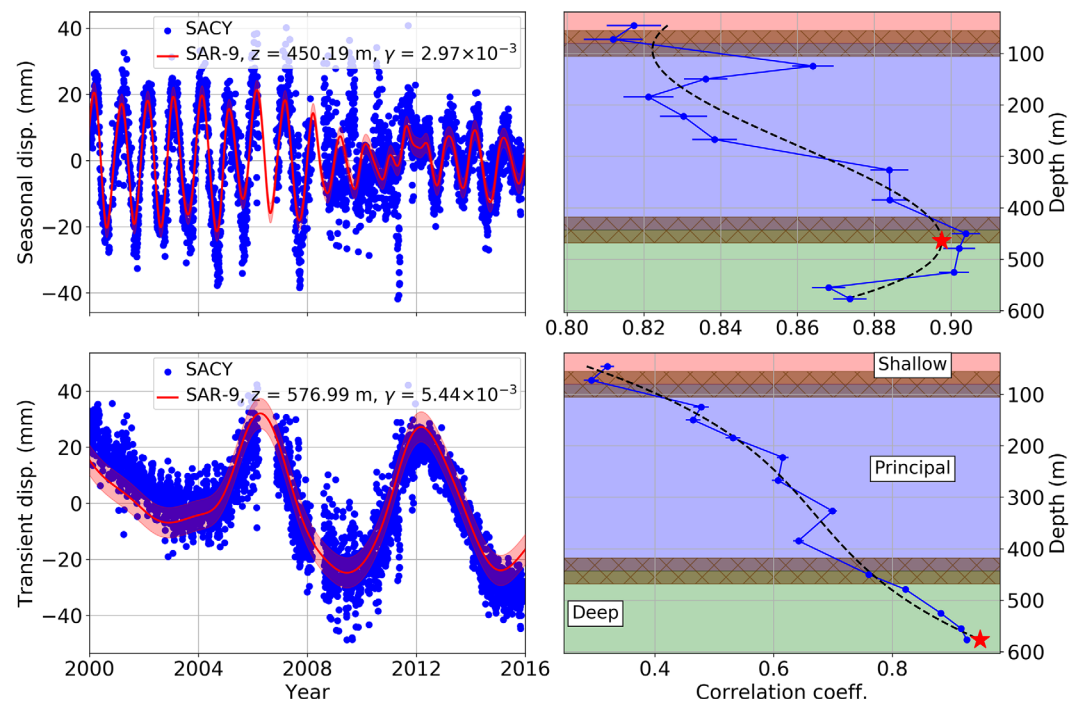
Figure 7. Cross correlation analysis between SAR-9 head data and SACY GPS data. The upper plots correspond to short-term, seasonal signals for both data sets while the lower plots correspond to long-term signals. We iterate over the time series at each port depth, compute the Pearson correlation coefficient between well and GPS data, and estimate the storage coefficient (scaling parameter) to best match the well and GPS data. We perform 100 bootstrap trials with random subsets of the data in order to estimate uncertainties in the correlation coefficients. The right plots show the mean Pearson correlation coefficient (and 95% confidence interval) between the time series at each port depth and the SACY GPS time series. The dashed black line corresponds to a third-order polynomial fit to the mean correlation coefficients, and the red star indicates the location of maximum correlation. The depths of best correlation are different for the short-term and long-term signals. For the left plots, SACY data are shown with blue dots and the scaled well data for the depth of maximum correlation are shown solid red lines. The optimal scaling factors are indicated by γ. The red shaded area represents the uncertainty in the scaling of the well data.

2012 (caused by a change in annual pumping practices) can be observed in the short-term GPS signal. Additionally, the long-term decrease in water levels and two periods of lower pumping activity due to greater water availability are manifested as vertical subsidence and uplift, respectively. We find that the seasonal ground deformation is best correlated with hydraulic head variations at a depth of about 450 m. Interestingly, the depth of best correlation for the long-term ground deformation is deeper ($\sim$580 m). In the next section, we perform a similar comparison of hydraulic head to ground deformation using an 18 year InSAR time series. The spatially dense observations provided by InSAR allow us to assess the time-dependent ground deformation at every well location, which is an advantage over the sparse GPS network over the coastal basins.

4. Central and Santa Ana Basin InSAR Time Series

We use 165 SAR acquisitions from the European Space Agency ERS (European Remote Sensing) and Envisat satellites spanning from 1992 to 2011 to form 881 interferograms. The maximum perpendicular baseline (spatial separation between orbits) is 480 m, which is reasonable for isolating ground deformation over metropolitan areas for C-band SAR instruments. The temporal repeat times range from 35 to 210 days, although after 1995, the repeat times are generally 35 or 70 days which is sufficient to model most deformation signals observed in the GPS data. We use a coherence threshold of 0.4 to mask poorly resolved areas (such as over water) and any areas with unwrapping errors. Interferometric phase contributions due to topography are removed using a digital elevation model (DEM) produced by the Shuttle Radar Topography Mission (SRTM) with approximately 30 m spacing (Farr et al., 2007). We estimate and remove phase delays due to atmospheric effects using global atmospheric reanalysis data from the European Center for Medium-Range Weather Forecasts (ECMWF; Jolivet et al., 2014). We also remove long-wavelength signals due to orbital errors by estimating a two-dimensional linear ramp for each interferogram. Finally, we reference the time series to a 400 m $\times$ 400 m window colocated with the SCIGN GPS station SNHS which is located in an area of high coherence showing stable ground motion unaffected by groundwater withdrawal (Figure 3).

4.1. Seasonal Amplitude and Phase Maps

We first reconstruct the InSAR time series using the same time parameterization approach as equation (13) where we assume the ground deformation can be described as a superposition of sinusoidal seasonal and transient effects and estimate the sinusoidal and B^i-spline coefficients independently for each pixel (Hetland et al., 2012). We limit our initial analysis of the InSAR time series to interferograms prior to 2008 to reduce the effect of changes in annual pumping practices on the time series reconstruction. In supporting information section S1 and section 5, we describe our method for performing a fully spatiotemporal time series analysis for the full time series to account for nonsteady seasonal and transient deformation. At this point, our primary goal is to examine the characteristics of the steady seasonal deformation prior to 2008, and our experiments show that a pixel-by-pixel approach is suitable for estimating the coefficients of the sinusoidal components. We can then generate maps of seasonal amplitude and phase using equation (15) for each pixel.

Maps of the estimated amplitude and phase for the seasonal signal between 1992 and 2008 show that most of the seasonal deformation is concentrated within the Los Angeles and Santa Ana Coastal Basins in the region corresponding to the confined aquifer system (Figure 8). The maximum peak-to-peak amplitude is 5 cm in the southern end of the Santa Ana Coastal Basin, which agrees with the results obtained by Bawden et al. (2001), Watson et al. (2002), and Lanari et al. (2004). We can also observe a smaller pair of high-amplitude regions closer to Long Beach with amplitudes of 3 cm. Here withdrawal occurs primarily at older sequences that have been folded up closer to the land surface. Low vertical permeabilities at these older, deeper sequences result in large water-level variations at these pumping sites in response to pumping stress. The seasonal amplitude decreases rapidly outside of the confined aquifer systems, particularly in the western edge of the basin bounded by the Newport-Inglewood Fault (NIF) where the fault is an effective barrier to across-fault fluid flow. This effect can also be observed in the map of the seasonal phase where the ground east of the NIF has a peak signal in March whereas the ground west of the NIF has a peak signal in July. The seasonal amplitude decreases rapidly to the north toward the forebay in Los Angeles where aquifers are semiconfined/unconfined, reducing the water-level response to groundwater withdrawal.
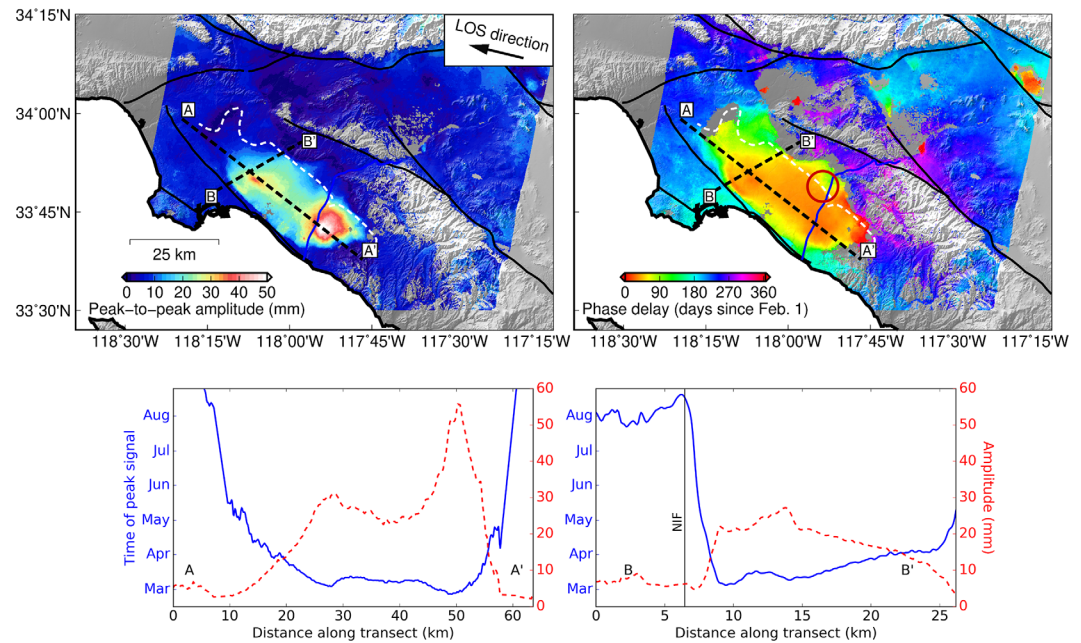
Figure 8. Maps of seasonal peak-to-peak amplitude and phase delay. The dashed black lines show the location of the transects used for the bottom plots. The dashed white line indicates the approximate boundary between the forebay and confined areas. The arrow indices the satellite-to-ground line-of-sight (LOS) direction. The red circle in the map of seasonal phase delay shows the location of a discontinuity in amplitude and phase within the basin. For the lower transect plots, blue lines correspond to the phase delay while the dashed red lines correspond to the peak-to-peak amplitude. In general, the deforming areas of the basin correspond to the confined aquifer system.

In general, the seasonal amplitude appears to be inversely correlated with the seasonal phase in the center of the basin, i.e., higher amplitude areas peak earlier in the year, which suggests that groundwater dynamics here follow a diffusion process. The central areas of the basin experience the highest amplitudes and earliest peak times, and we observe delays as one moves toward the margins of the basin. From section 3.2, we observed a similar delay in hydraulic head from the well data, suggesting that the main driver of the delay in ground deformation in the central regions of the basin is the time delay necessary for aquifer pressures to equilibrate in the horizontal direction in response to pumping. Furthermore, in the northwest area of the basin where aquifer thicknesses are relatively uniform, we can observe an exponential decline in seasonal amplitude and linear variation in seasonal phase away from an amplitude peak (A–A′ transect in Figure 8), which agrees with the diffusion solution for periodic head variations in equation (11). As with the well data,
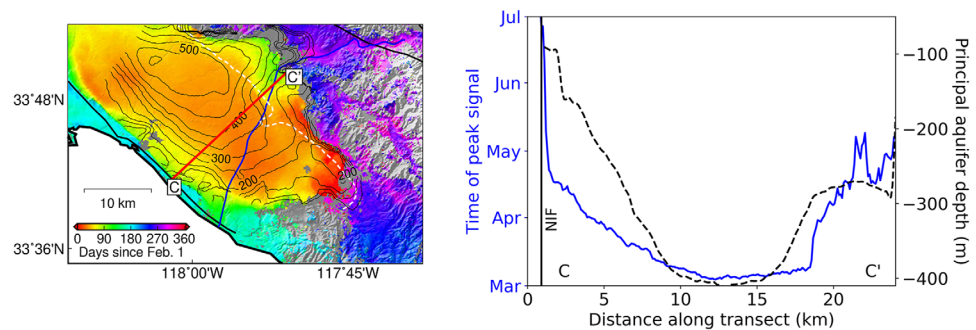

Figure 9. Map of seasonal phase delay (left) with contour lines and labels corresponding to the depth of the bottom of the principal aquifer system in meters. The dashed white line corresponds to the approximate boundary between the forebay and confined areas as defined by OCWD. The solid blue line corresponds to the Santa Ana River. The right plot shows the transects (C–C′) for the seasonal phase (solid blue) and aquifer depth (dashed black). While there appears to be a general trend between depth of the principal aquifer system and seasonal phase delay, several other factors control spatial propagation of hydraulic head (see section 6.3).

the boundaries of the deforming areas become more difficult to interpret due to the transition from confined aquifer units to unconfined/semiconfined units.

We also observe a sharp discontinuity in both the seasonal amplitude and phase maps on the eastern edge of the basin where the Santa Ana River enters the forebay region indicating some form of impediment to groundwater flow. Here the peak amplitude occurs in March on the west side of the discontinuity and in May on the east side. In section 3.2, we discussed the possible influence of specific yield contrasts and faults acting as impediments to fluid flow. While no known faults exist in this area, this area also corresponds to the approximate boundary between the forebay and confined zones. Comparison of the seasonal phase map to the thickness of the principal aquifer system (using the aquifer model developed by OCWD) shows that the phase discontinuity is also roughly coincident with large changes in depth of the principal aquifer system in the OCWD model across a short distance (Figure 9). In section 6.3, we explore dynamic models investigating the impact of variations in aquifer thickness on propagation of hydraulic head.

4.2. Groundwater Withdrawal and Seasonal Ground Deformation

We expect that groundwater pumping practices would have a strong impact on the amplitude of seasonal ground deformation. Hydraulic head in a confined aquifer system near a production well will experience a drawdown during periods of groundwater withdrawal (Middleton & Wilcock, 1994; Todd & Mays, 1980). To explore the impact of withdrawal on head levels, we use groundwater production time series for 250 OCWD production wells that measure total groundwater withdrawal on a monthly basis from 1996 to 2007. We create a 50×50 uniform grid where the dimension of each grid cell is approximately 0.6×0.6 km and compute the amplitude of total seasonal groundwater withdrawal in each grid cell. We perform this procedure for three different depth ranges (0–200, 200–370, and 370–700 m depth) to explore the depth dependency of withdrawal. We can clearly observe an association between the high ground deformation areas and areas with high seasonal groundwater production at depths mostly associated with the principal aquifer system (Figure 10). The pair of high-amplitude ground deformation regions near Long Beach directly correspond to two regions of concentrated groundwater withdrawal between 200 and 370 m depth. However, not all areas of high groundwater withdrawal are colocated with high ground deformation, particularly
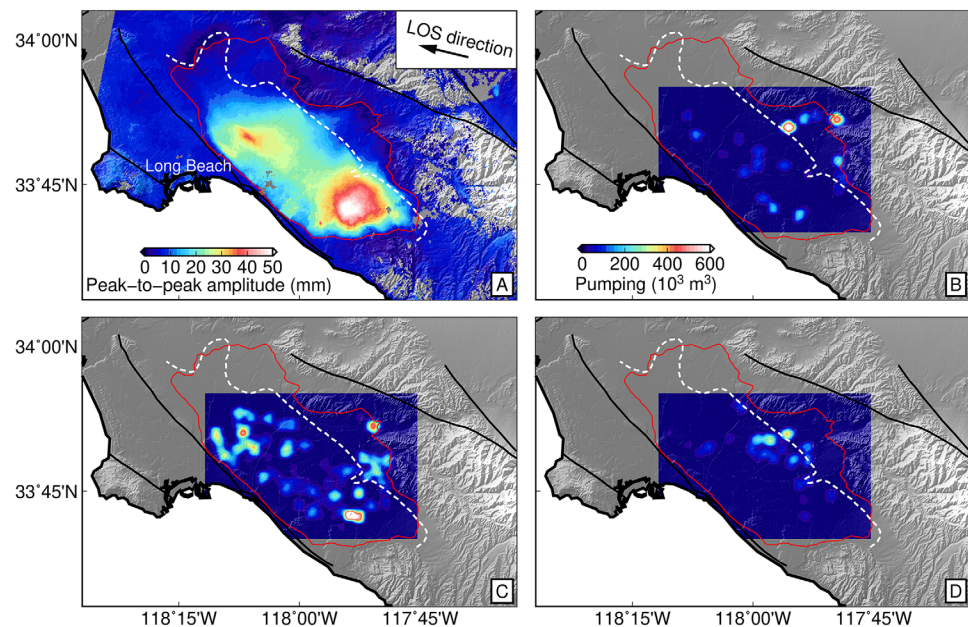
Figure 10. Maps of (a) seasonal peak-to-peak LOS amplitude and seasonal groundwater withdrawal from OCWD production wells located at depths of (b) 0–200 m, (c) 200–370 m, and (d) 370–700 m. See supporting information Figure S2.4 for the corresponding seasonal phase delays. The locations with the highest seasonal withdrawal at 200–370 m depth correspond to the locations of the highest seasonal ground deformation within the pressure area. The red outline encompasses the seasonal ground deformation as observed in the InSAR map of seasonal phase delay. The dashed white line indicates the approximate boundary between the forebay and confined areas. In general, the areas of highest seasonal ground deformation correspond to locations where confined aquifers are most heavily pumped.

in the forebay regions. In those regions, the shallow aquifers are heavily pumped (e.g., Figure 10b) but are unconfined, and the principal aquifer system is semiconfined (Woodside & Westropp, 2015). Since both aquifer zones have large storage coefficients in the forebay, large fluctuations in groundwater production will result in smaller fluctuations in groundwater levels as compared to the center of the basin. Related to the seasonal ground deformation phase delay, groundwater production peaks during the summer months at roughly the same time for nearly all large-scale production wells (supporting information Figure S2.4). This uniformity removes variability in pumping times as a driver for spatial variations in seasonal ground deformation phase delay, leaving aquifer geometry and storage variations as the primary remaining factors controlling the propagation of hydraulic head (discussed in section 6.3).

5. Simultaneous Time-Varying Seasonal and Long-Term Ground Deformation Using InSAR Time Series Analysis

In order to study the full complexity of ground deformation in the Central and Santa Ana Coastal Basins, including the time-varying seasonal deformation and long-term subsidence, we now decompose the full InSAR time series from 1992 to 2011 into seasonal and transient components using a new method for geodetic time series analysis that extends on the sparse regularization methods of Riel et al. (2014) by incorporating spatial coherency into the time series reconstruction (see supporting information section S1). This method estimates the coefficients of a temporal dictionary for every pixel simultaneously, resulting in a very large regularized least squares problem that uses data from all interferograms. The regularization function for the model parameters is a combination of a sparsity-inducing ℓ_1-norm (to isolate the dominant onset times and durations of any transient signals) and an ℓ_2-norm (for parameters that may be correlated in space or time). We adapt a distributed convex optimization algorithm, the alternating direction method of multipliers (ADMM), to solve this problem in parallel using hundreds of CPUs. This algorithm allows us to solve a least squares problem with several million parameters in only a few minutes; the end result is a self-consistent time series model that can be decomposed into long-term and short-term signals of various time scales.

Prior to the time series decomposition, we limit the area of analysis to the coastal basins and downsample the pixels to a spacing of approximately 200 m in order to reduce the computational load. We then populate the temporal dictionary with third-order B-splines with time scales of 0.2 years to model the seasonal ground oscillations caused by the annual cycle of groundwater withdrawal and recharge. Similar to the decomposition of the SACY GPS data in section 3.3, we include coherency between B-splines that share the same centroid time within a year (in addition to the spatial coherency). We also include B^i-splines in the temporal dictionary to model long-term, transient signals.

To validate the estimated InSAR time series model, we compare the decomposed long-term and short-term signals with long-term and short-term signals measured by three GPS stations within the Santa Ana Coastal Basin. We use the method of Riel et al. (2014) to perform the time series decomposition for the GPS time series independently from the InSAR time series. As with the InSAR data, we use B-splines for seasonal signals and B^i-splines for long-term signals with a sparsity-promoting regularization scheme to limit the total number of B^i-splines needed for reconstruction of the GPS data. We then project the three-component GPS time series onto the radar LOS direction. The long-term and short-term signals from the two data sets are in good agreement, even during time periods where we have a gap in temporal coverage of SAR acquisitions (Figure 11). Slight spatial oversmoothing for the InSAR data has the effect of damping the amplitudes of the seasonal oscillations, leading to small seasonal oscillations in the short-term residuals (residuals also tend to be larger during periods with a lower number of SAR acquisitions). As expected from the SAR-9 head time series, the short-term, seasonal ground deformation is relatively steady from 1996 to 2000, followed by a slight decrease in amplitude of oscillations from 2000 to 2007. After 2007–2008, the seasonal signal changes its temporal pattern significantly as a result of the cessation of water storage programs that encouraged regular, increased groundwater withdrawal during the summer months. These changes can also be observed in the GPS time series. The long-term signal once again shows long-term subsidence which is interrupted by a 2 year uplift period between 2004 and 2005. In the following sections, we use the spatial continuity of our InSAR time series model to examine the spatial behavior of the unsteady seasonal signals, as well as the long-term subsidence and transient uplift caused by decreased pumping activity.
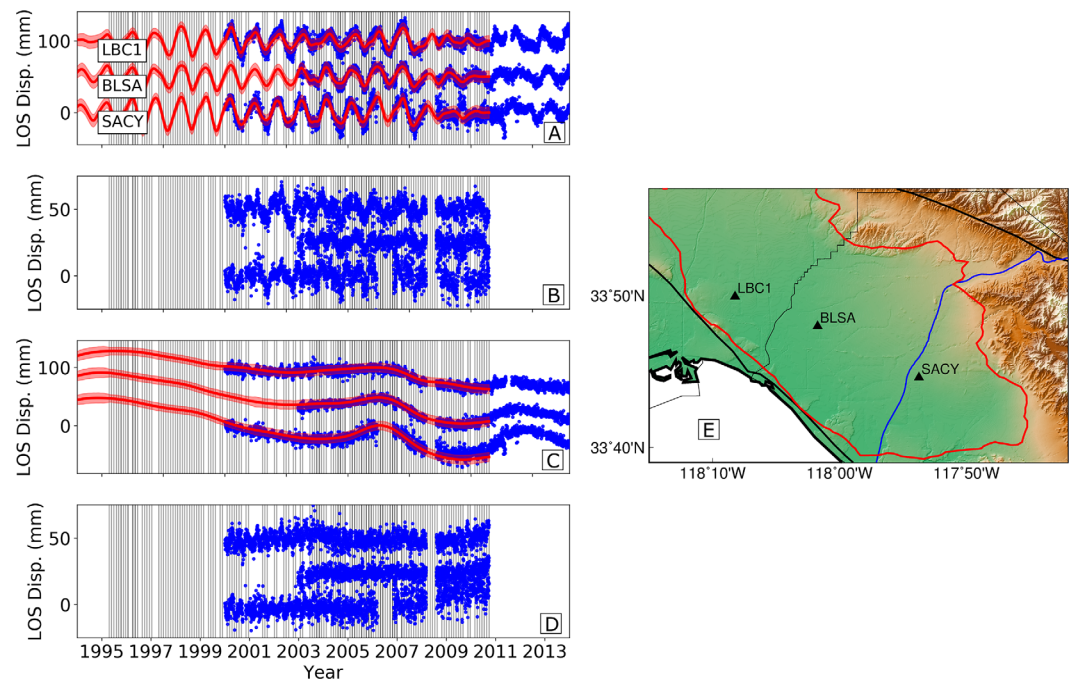
Figure 11. InSAR time series reconstruction compared with three GPS stations (LBC1, BLSA, and SACY) in the basin. The GPS data are projected onto the radar LOS direction; time series for all plots are shown with offsets for visual clarity. Both the InSAR and GPS time series have been decomposed into (a) short-term, seasonal signals and (c) long-term, transient signals. GPS data are shown with blue dots, and InSAR data are shown with solid red lines. The shaded red regions in Figures 11a and 11c represent the uncertainties in the reconstructed InSAR time series. Note the increase in uncertainty during time periods with no SAR acquisitions. Thin vertical black lines correspond to the SAR acquisition times. (b, d) The residuals between the GPS and InSAR data in Figures 11a and 11c, respectively. The locations of the GPS stations are shown in (e).

5.1. Short-Term Basin Deformation

We isolate the short-term basin deformation using the B-spline coefficients estimated from the InSAR time series analysis and compare the March to September ground deformation for three different years: 2004, 2008, and 2009 (Figure 12). For 2004, the March to September basin subsidence is in good agreement with the seasonal amplitude map in Figure 8, which is expected since annual pumping practices were very regular during this time period. Peak subsidence is greater than 40 mm in the southeast zone of the Santa Ana Coastal Basin. However, in 2008, we observe a significant reduction in ground deformation throughout the whole basin. Peak subsidence only reaches 10–15 mm primarily in areas closer to the coast and in the center of the basin. In 2009, the spatial pattern changes again, with peak subsidence now reaching about 30 mm in a concentrated zone in the southern edge of the basin close to the main source of groundwater
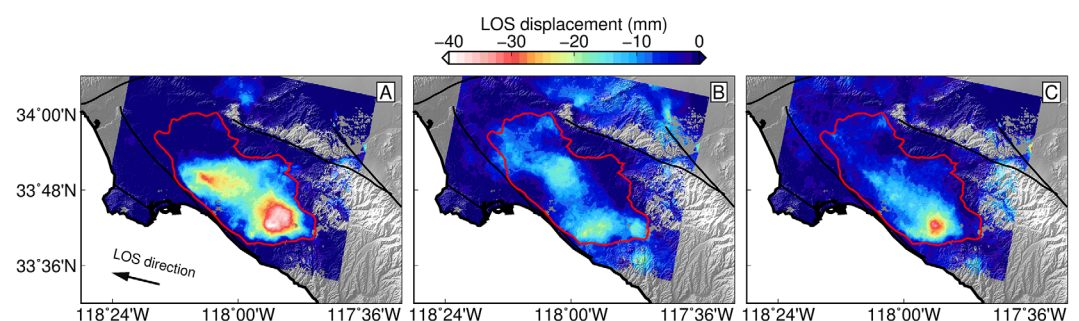

Figure 12. Maps of March to September LOS deformation for three different years: (a) 2004, (b) 2008, and (c) 2009. The 2004 ground deformation is consistent with the maps of seasonal amplitudes, whereas the 2008 and 2009 maps show starkly different spatial patterns and amplitudes due to changes in pumping practices.

withdrawal. For both 2008 and 2009, we see that most of the seasonal ground deformation closer to Long Beach in the western half of the basin disappears, and most of the deformation in the forebay region is minimized as well.

5.2. Long-Term Basin Deformation

By examining the spatial distribution of the B^i-spline coefficients as estimated by the ADMM time series analysis, we can determine the onset times and durations of the dominant long-term, transient signals in our time series. The sparsity-promoting regularization forces most of the coefficients to be zero except for those associated with several longer-term deformation signals observed primarily within the coastal basins (supporting information Figure S2.1). First, we detect a ∼2.5 year subsidence signal starting in 2007 that is contained within the region of the basin defined by the phase delay of the seasonal deformation. From the comparison between GPS and hydraulic head data in section 3.3, it is likely that a large fraction of this observed subsidence is due to an overall reduction in groundwater levels in the principal and deep aquifer systems. The subsidence was preceded by a 2–3 year uplift signal in the southeastern portion of the Santa Ana Coastal Basin starting in late 2004, which we observed in the data for GPS station SACY and is due to a period of decreased pumping due to greater water availability during the winter of 2004–2005 (Figure 4). This period of greater water availability has also been associated with transient uplift due to recharging aquifers in nearby basins (King et al., 2007).

Profiles of the deformation patterns for the three main long-term events (1995–2004 subsidence, 2004–2007 uplift, and 2007–2010 subsidence) suggest that the two subsidence periods are connected and act as a single subsidence process that is distinct from the uplift period due to decreased pumping activity (Figure 13). The subsidence is strongest in the center of the basin and is roughly coincident with the area of high seasonal deformation. Additionally, we observe that the subsidence rate increased by a factor of 2 after 2007. The strongest subsidence signal actually occurs within two narrow regions of the southeastern basin with length scales of approximately 3–5 km. In these regions, the subsidence rate was 15 mm/yr between 1995 and 2004 and nearly 30 mm/yr between 2007 and 2010. The rest of the subsidence is broadly distributed throughout the rest of the basin. During the uplift event, most of the uplift is concentrated on the
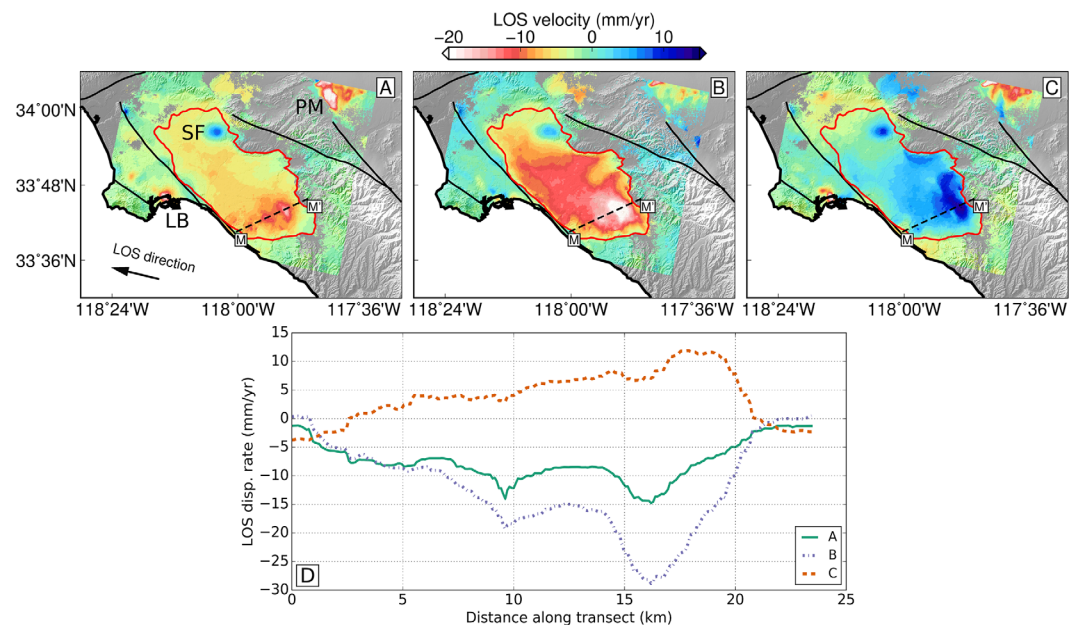

Figure 13. (a–c) Maps of subsidence and uplift rates for the time periods (a) 1995–2004, (b) 2007–2010, and (c) 2004–2007. The labels in Figure 13a indicate the subsidence in Long Beach (LB) due to the Wilmington oil Field, uplift in the Sante Fe Springs Oil Field (SF), and subsidence in Pomona Basin (PM) due to groundwater withdrawal. The transect profile is shown by the black dashed line, M–M′. (d) The solid green line corresponds to the transect for the 1995–2004 time period, and dashed blue line corresponds to 2007–2010, and the red dashed line corresponds to 2004–2007. The transect data show very consistent deformation rate profiles for the two time periods associated with subsidence, whereas the uplift profile has a distinctly different profile.

eastern margin of the basin where we observe ∼30 mm of uplift. This area of the basin is where the Santa Ana River flows into basin and is close to the main point of entry for artificial recharging operations. This area is also coincident with the forebay area of the basin which is a mix of semiconfined (principal) and unconfined (shallow) aquifers (Woodside & Westropp, 2015). The concentration of uplift in this region is coincident with recharge in the shallow and principal aquifer systems due to decreased withdrawal and greater water availability.

We can also observe long-term signals from 1995 to 2004 not associated with groundwater activities in the coastal basins, such as uplift in the Santa Fe Springs Oil Field and subsidence in the Wilmington Oil Field in Long Beach. For the latter, episodic subsidence has been observed due to historically high oil production despite modern re-pressurization efforts (Hauksson et al., 2015). For the former, the uplift mechanism is unclear since extraction rates have generally been higher than injection rates which would usually lead to net subsidence (Bawden et al., 2001). We can also observe subsidence in the Pomona Basin due to groundwater withdrawal. We do not observe large tectonic signals from fault slip due to the high-subsidence rates in the basin. The NIF is perhaps the best observed fault system in this data set due to high interferometric correlation, and it is estimated to have a slip rate of approximately 1 mm/yr which is likely to be obscured by the groundwater-driven subsidence in the basin (Bawden et al., 2001; Zhang et al., 2012).

The modeled transient time series for points within the narrow, high-subsidence areas exhibit much more rapid subsidence than representative points in other regions of the basin (Figure 14). For the eastern high-subsidence zone (represented as point (i) in Figure 14), the subsidence monotonically increases after 2007 while the western high-subsidence zone (point (iii)) appears to reverse its subsidence signal similar to the rest of the basin. By comparing the spatial pattern and location of these high-subsidence areas to the seasonal amplitudes and time to peak seasonal signal, it is clear that the subsidence process for these areas is
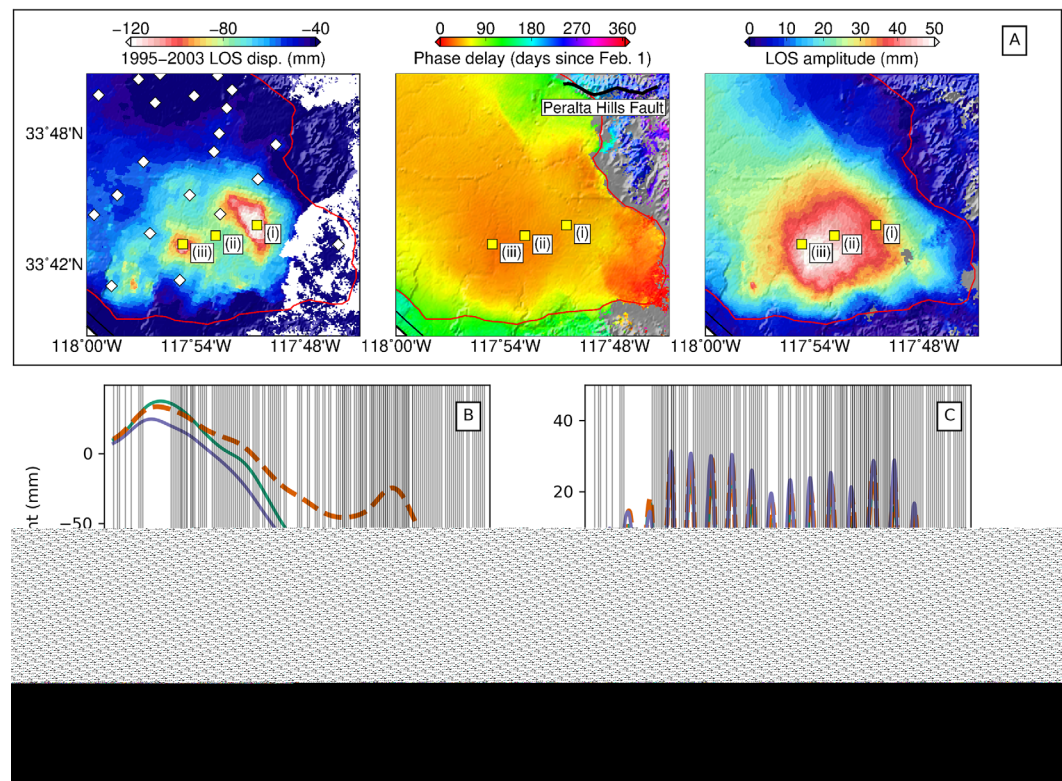

Figure 14. (a) Close-up maps of long-term LOS displacement from 1995 to 2004, seasonal phase delay, and seasonal peak-to-peak amplitude. The white diamonds in the subsidence map correspond to large-scale OCWD production wells. The yellow squares show the locations of the time series in (b) and (c). (b) The time series for the long-term displacements while (c) shows the time series for the short-term, seasonal displacements. Note the location of the Peralta Hills thrust fault in Figure 14b discussed in section 6.3. While the short-term time series for all three points are very similar, the long-term signals within the zones of high subsidence are noticeably different than the point between them.

not adequately explained by an elastic response due to the hydrological cycle of groundwater recharge, withdrawal, and steady decline. In fact, the seasonal time series for points within and adjacent to the high-subsidence areas are nearly identical (Figure 14c). We had previously observed that the long-term ground deformation for the GPS station SACY can be fully explained by long-term changes in groundwater levels in the principal and deep aquifer systems (Figure 7). Unfortunately, SACY and other OCWD wells lie just outside the high-subsidence regions, preventing us from determining whether rapid decline of water levels is responsible for the large ground deformation there. However, the small spatial wavelength of these features (2–3 km wide) suggests that the subsidence mechanism may be due to long-term, inelastic compaction of aquitards or laterally compact clay lenses in the aquifers rather than a diffusion-based response to withdrawal, which has a characteristic spatial scale of 10–20 km (Figure 8).

The long-term subsidence signals for both 1995–2004 and 2007–2010 and the seasonal ground deformation amplitude show relatively consistent spatial patterns characterized by peak ground deformation in the southeast area of the basin and larger deformation in the center of the basin as compared to the margins (Figure 13). In order to analyze the differences in the spatial patterns of the two signals, we first estimate the optimal scale factor for the seasonal ground deformation that minimizes the difference between the seasonal amplitude and long-term subsidence signal from 1995 to 2004. After applying the optimal scale factor (approximately -4) to the seasonal amplitudes, we can create a map of *residual* subsidence to isolate the differences between the long-term and short-term signals (Figure 15). The residual subsidence along the margins of the basin shows that the spatial extent of long-term ground subsidence is larger than the extent of seasonal ground oscillation. The areas of residual subsidence are also not exclusively in the forebay, suggesting that the transition from confined to unconfined aquifers is not the primary mechanism for the wider extent of subsidence. While it is possible that inelastic deformation may be occurring to a greater degree along the margins, there is insufficient evidence to suggest richer clay content in those areas. Instead, we propose that the dependency of hydraulic head variations on the temporal frequency of groundwater withdrawal can explain the residual subsidence along the margins (see section 6.2 for further discussion).

Of the two narrow zones of high-subsidence shown in Figure 14, only the larger zone is noticeable in the residuals, suggesting that the smaller subsidence zone may simply be responding elastically to long-term declines in groundwater levels. The persistence of the larger high-subsidence zone in the residuals supports the idea that this feature is caused by long-term, inelastic compaction of clay lenses since this localized area does not correspond to any large-scale production wells. In summary, the long-term ground deformation we observe with InSAR exhibits distinct spatial and temporal characteristics when compared with short-term, seasonal deformation, which could be indicative of compaction of a different region of the aquifer system or potentially large-scale inelastic compaction if long-term ground deformation is not directly
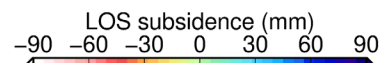

Figure 15. Comparison between long-term LOS subsidence from (a) 1995 to 2004 and (b) residual subsidence after removing a synthetic subsidence signal corresponding to the scaled seasonal displacement. The red outline encompasses the seasonal ground deformation as observed in the InSAR map of seasonal phase delay. The dashed white line indicates the approximate boundary between the forebay and confined areas. The residuals indicate that the spatial extent of long-term ground subsidence is larger than the extent of seasonal ground oscillation.

correlated to long-term groundwater-level declines (e.g., sustained subsidence even after recovery of groundwater levels).

5.3. Ground Deformation Versus Hydraulic Head for the Santa Ana Coastal Basin

In section 3.3, we compared hydraulic head time series from OCWD well SAR-9 with vertical ground deformation time series from GPS station SACY and found that short-term, seasonal ground deformation was most correlated with short-term head variations near the aquitard layer separating the principal and deep aquifer systems. On the other hand, long-term ground deformation was most correlated with long-term head variations in the deep aquifer system. We expand on that analysis by comparing InSAR-derived ground deformation to the OCWD wells within the deforming areas of the coastal basins (we exclude the WRD wells in this analysis because there are no water-level data prior to 2000). For each well location, we iterate over the hydraulic head time series for each port depth and compute the correlation coefficient with the InSAR-derived ground deformation. We then use a third-order polynomial to estimate the depth of maximum correlation for both seasonal and long-term deformation.
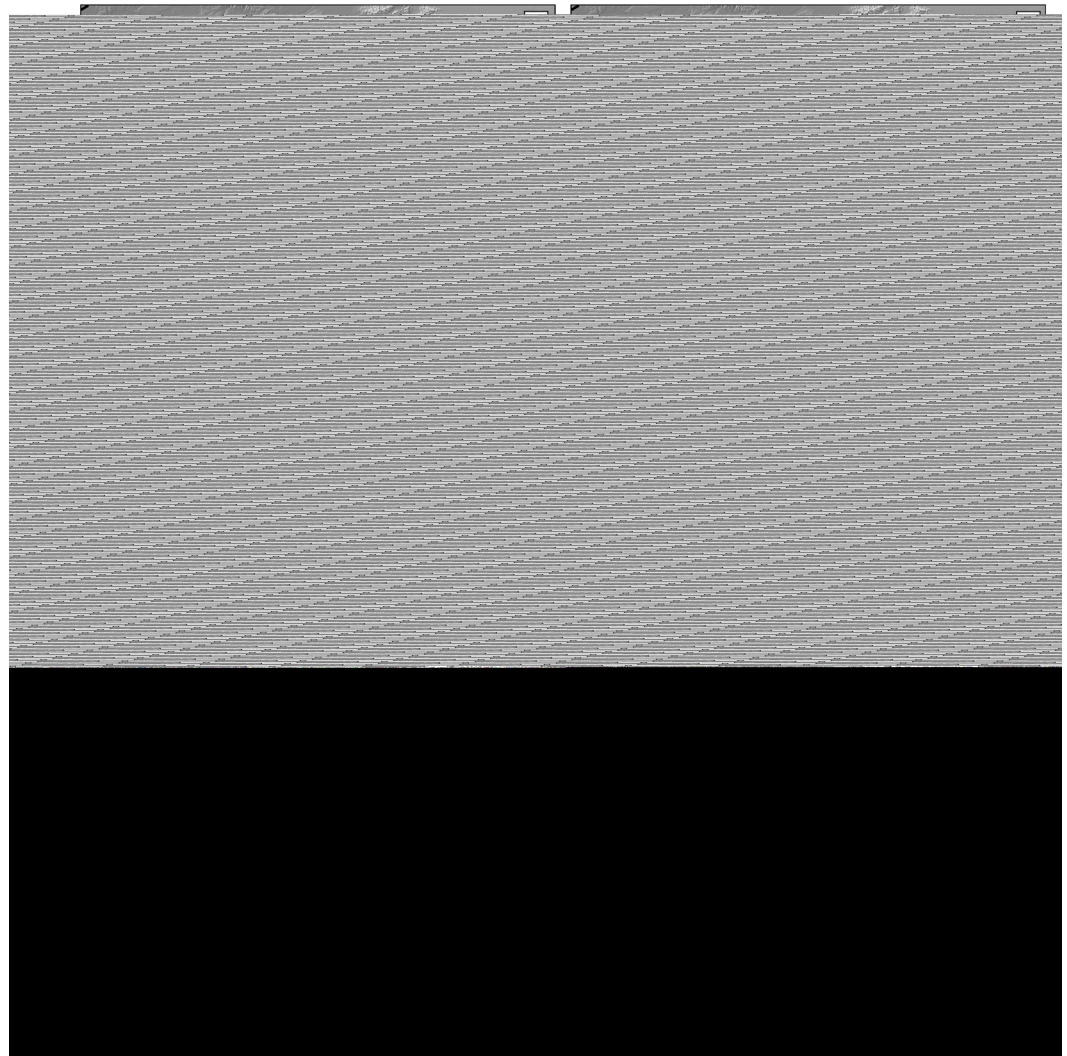

Figure 16. Depth of maximum correlation between hydraulic head data and InSAR displacement are denoted with colored circles for OCWD wells for (a) seasonal signals and (b) long-term signals. The background color in the basin corresponds to the depth of the bottom of the principal aquifer system. (c–f) The InSAR time series (blue) and scaled head for the well port with maximum correlation (red) for select wells in the basin. Optimal scaling factors for hydraulic head are indicated by γ. The depths of best correlation for the seasonal signals are systematically shallower than those for the long-term signals.

For both seasonal and long-term signals, the depths of the well ports most correlated with ground deformation are deeper in the center of the basin than in the margins, which roughly follows the geometry of the principal aquifer system (Figure 16). For seasonal signals, the depth of best correlation is generally at depths associated with the largest amount of groundwater withdrawal in the principal aquifer system, similar to the SACY and SAR-9 comparison. Furthermore, the depth of best correlation for the long-term signals is systematically deeper throughout the basin and primarily within the "deep" aquifer system. We note that since monitoring wells do not fully penetrate the entire aquifer system, the true depth of best correlation for the long-term signals may be deeper than the ones shown here. While the seasonal deformation is well-matched by the scaled head data, there are some noticeable discrepancies between the long-term signals. Mainly, there appears to be a lag between the ground deformation and the hydraulic head, which can likely be attributed to the truncated sampling of the deep aquifer system by the monitoring wells (see section 6.2 for further discussion). At a minimum, the hypothesis that the observed ground deformation within the coastal basins is an elastic response to changing groundwater levels appears to be true for the seasonal signals and a significant fraction of the long-term signals (with the exception of the narrow, high-subsidence zones discussed in the previous section).

6. Discussion

6.1. InSAR and Groundwater Management

The total level of seasonal groundwater withdrawal by OCWD is well correlated with seasonal changes in hydraulic head in the principal aquifer system. As a consequence, the areas with the highest levels of seasonal groundwater withdrawal directly correspond to the areas with the highest amplitude of seasonal ground deformation (Figure 10). We also observed that due to changes in pumping practices in 2008 by major water districts (where prior to 2008, pumping was encouraged during the summer months), the spatial pattern of ground deformation during the summer months changed drastically. To compare the overall relationship between groundwater withdrawal and basin deformation, we use the long-term and short-term InSAR results to construct time series of spatially integrated basin deformation. Similarly, a time series of total groundwater production is constructed from the OCWD production wells and decomposed into long-term and short-term signals using the same method used for the SAR-9 time series.
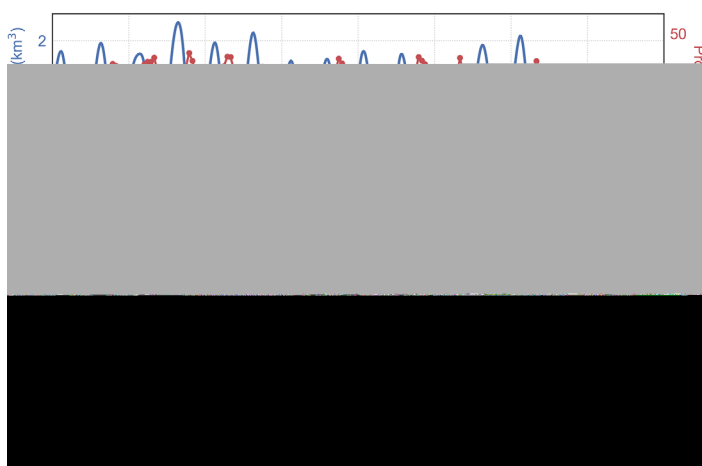
Figure 17. Time series of total volumetric basin deformation vs. total monthly OCWD groundwater production for (a) seasonal signals and (b) long-term signals. The solid red line with red circles represents the total reported groundwater production in 1 month intervals. The volumetric basin deformation was computed by summing the product of pixel area and displacement at each pixel. The dashed red lines correspond to a model of the production time series consisting of annual and semiannual sinusoids for Figure 17a and B^i-splines for Figure 17b. In Figure 17b, the data are not shown for visual clarity, and the red shaded area indicates the 1-sigma scatter of the data. In general, groundwater levels show a delayed response to changes in groundwater production; the delay for long-term signals is longer than for short-term signals.

As expected, the seasonal basin deformation is out of phase with the seasonal groundwater production by about 4–5 months (Figure 17). Ground uplift reaches peak levels around March after several months of low groundwater production. Peak groundwater production then occurs in July/August, although production is generally high between May to September. Peak production is then followed by maximum seasonal ground subsidence around September. The long-term subsidence signals are relatively consistent with the long-term variation in groundwater production. However, a time lag of of about two years can be observed between the basin ground deformation and groundwater production, which is consistent with the InSAR results at specific wells in the previous section. From 1995 to 2002, a steady increase in production corresponded to steady subsidence within the basin. The basin uplift initiating in 2005 is a net response to greater water availability (Figure 4) and decreased production, both of which led to historically high water levels (Woodside & Westropp, 2015). The increased basin subsidence rate following the uplift appears to be a (lagged) response to an increase in production rate starting in late 2005. Therefore, we conclude that the majority of both the long-term and short-term ground deformations are elastic responses to changes in head levels caused by changes in total groundwater production and recharge. The consistency between deformation and head levels, and the lack of evidence of any large-scale inelastic compaction, requires that storage coefficients generally remain constant in time, which means that stress levels within the aquifer and aquitards have

remained above preconsolidation levels since the 1990s (with the exception of the high-subsidence zones identified in Figure 14). Historical water levels from OCWD forebay monitoring wells show that the lowest water levels occurred around 1950, and modern water levels have generally remained stable since then (supporting information Figure S2.3).

6.2. Estimating Depth-Dependent Storage Coefficients

Estimation of storage coefficients for the multiaquifer systems in the Central and Santa Ana Coastal Basins is complicated by the fact that ground deformation is the integrated compaction with depth of all aquifer and aquitard layers. From Figure 2 and geologic cross sections throughout the basin (Ehman et al., 2014), we also know that the aquifer and aquitard structure is fairly complex. For many of the monitoring wells in the groundwater basins, the ports do not span all of the main aquifer layers, so we cannot fully assess the contribution of each layer to the observed ground deformation in the presence of appreciable head variability in depth. However, the hydraulic head data for most monitoring wells show that the bulk of the seasonal variations occur within the principal aquifer system. Compared to long-term variations, the seasonal hydraulic head amplitudes show greater attenuation with vertical distance from the principal aquifer system (Figures 5 and 7). From equation (11), a lower temporal frequency for a period pressure perturbation will result in a lower attenuation of amplitude and a slower diffusion speed. Thus, long-term pressure changes cause greater overall pore pressure changes for the deep aquifer system than the seasonal signals. This interpretation is consistent with the fact that there is very little direct withdrawal at the depths of the deep aquifer system (Figure 10). Therefore, estimation of depth-dependent storage coefficients is likely to be more reliable when analyzing the seasonal oscillations in hydraulic head since errors due to truncated sampling of the deep aquifer system are minimized. For this analysis, we compare hydraulic head from the OCWD well SAR-9 to vertical ground deformation from the GPS station SACY since SAR-9 spans all relevant aquifer layers.

For a vertical profile of the multiaquifer system discretized onto a uniform grid, we can express the ground deformation at the surface as

$$\Delta d = \sum_{i=1}^{5} S_{S_k^i} \sum_{j=1}^{N_i} \Delta h_j \Delta z, \tag{17}$$

where $S_{S_k^i}$ is the skeletal specific storage for the ith layer which consists of N_i elements of uniform thickness Δz, and h_j is the hydraulic head for the jth element in layer i. Here we use the OCWD approximation and assume five total layers (three aquifer system layers and two aquitards) with depths specified by the OCWD aquifer model. While this model is a significant simplification of the true aquifer structure, reasonable similarities in hydraulic head time series for wells within a given OCWD layer suggest that this simplification is appropriate for modeling the surface response. Since monitoring wells only coarsely sample the aquifer layers, at each observation epoch we interpolate the hydraulic head to a regular depth grid before computing $\sum_j \Delta h_j$ for each layer. We can then estimate the skeletal specific storage for all layers using linear least squares with a positivity constraint. Using equation (6), the skeletal specific storage can be converted to the skeletal storage coefficient S_k by multiplying the $S_{S_k^i}$ values by the thicknesses of the corresponding layers.

The predicted deformation from the seasonal hydraulic head variations closely matches the observed seasonal ground deformation (Figures 18a and 18c). The primary nonzero estimated storage coefficients correspond to the aquitard separating the principal and deep aquifer systems (about 2×10^{-3}) and the deep aquifer system itself (about 1.5×10^{-3}; Figure 18e). However, due to the poor constraints on the aquifer and aquitard boundaries and the coarse sampling of the monitoring ports in depth, it is possible that the value of the storage coefficient for the aquitard actually corresponds to the value for the principal aquifer system. The estimated storage coefficient values (2×10^{-3} and 1.5×10^{-3}) are similar to the storage coefficient values for the principal and deep aquifer system, respectively, estimated by OCWD from aquifer test data (Woodside & Westropp, 2015). We can use these storage coefficients to then predict the expected long-term ground deformation from the long-term hydraulic head variations (Figure 18b). Compared to the seasonal variations, long-term residuals are significantly more systematic and similar in temporal structure to the long-term signal itself (Figure 18d). If instead the residuals showed steady subsidence, then it would be likely that inelastic compaction was occurring as a background subsidence process. However, the temporal pattern of the residuals is more suggestive of a time lag between the predicted and observed ground
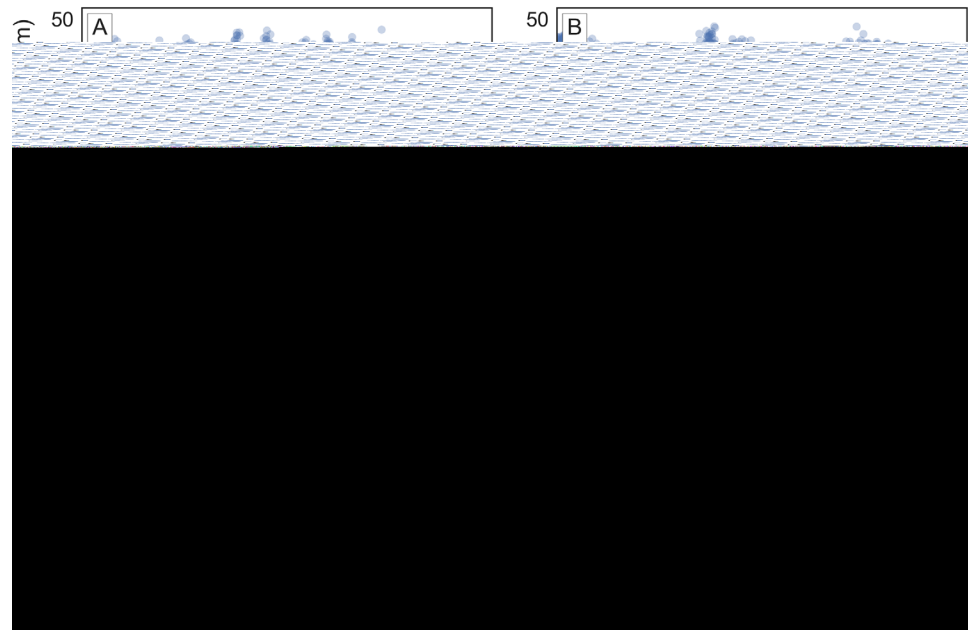
Figure 18. Estimation of storage coefficients for each aquifer system and aquitard layer using vertical seasonal ground deformation from GPS station SACY and seasonal hydraulic head from OCWD well SAR-9 (e). The estimated storage coefficients are used to predict deformation for (a) short-term seasonal and (b) long-term variations. GPS data are shown in blue dots while the prediction is shown in red. (c, d) The residual seasonal and long-term ground deformation, respectively, after subtracting the predicted deformation from the observed GPS data. The black line in Figure 18d corresponds to the smoothed long-term residuals for visualization clarity. While the short-term seasonal signals are well predicted by seasonal hydraulic head changes, systematic residuals in the long-term signal may reflect inadequate sampling of the deep aquifer system by the SAR-9 well.

deformation. When groundwater levels start to recover after a period of decline (e.g., around 2003, 2008, and 2014), the ground is predicted to uplift. Instead, the GPS time series shows a small period of continuing subsidence which is consistent with continuing decline of hydraulic head in the deeper regions of the deep aquifer system not measured by monitoring wells (and thus not accounted for in the predicted displacement). Additionally, the time lag may also be indicative of a greater degree of compaction due to clay interbeds and aquitards in the deep aquifer system.

For comparing ground deformation to hydraulic head throughout the groundwater basins, the complexity of the aquifer system (discontinuous aquitards, folding of aquifer units along the margins, etc.) limits our ability to reliably estimate storage coefficients for the simplified five-layer OCWD model even when restricting the analysis to seasonal signals. Instead, we used an alternative approach of estimating a depth for each well that resulted in the highest correlation between deformation and head. We found that the short-term, seasonal ground deformation was most correlated with wells that were located close to the bottom of the principal aquifer system. The high similarity between short-term head time series in the principal aquifer system (Figure 7) and fast diffusion speeds (Figure 5) indicate that seasonal ground deformation can probably be explained as a combination of bulk deformation of the principal aquifer system and compaction of aquitards located near the bottom of the principal aquifer system. We also found that a large area of the long-term subsidence signal was most correlated with wells located in the deep aquifer system, which again supports the hypothesis that the lower temporal frequency of the long-term pressure perturbation causes greater pressure changes in the deep aquifer system. In the horizontal direction, it was also observed that the spatial extent of the long-term subsidence was greater than the seasonal ground deformation (Figure 15). This observation would also be consistent with the long-term increase in groundwater production resulting in a larger areal extent of hydraulic head decline than the seasonal oscillations. Therefore, we can interpret the long-term decline in head level in the deep aquifer system as a delayed response to long-term variations in groundwater levels, which are driven by a combination of long-term variations in groundwater production due to variations in rainfall and overall water availability.

The narrow, high-subsidence regions shown in Figures 13 and 15 may correspond to inelastic compaction of laterally finite clay lenses in one of the aquifer system layers, particularly the larger of the two subsidence regions. The high amplitude of subsidence may also indicate that these clay lenses are substantially thicker than other compressible clay units within the aquifers. This region does not correspond to any large-scale production wells or significant withdrawal at any depth (see Figure 10), so the higher subsidence rate is most likely not caused by pumping activity since the 1990s. Instead, we are most likely observing a combination of inelastic compaction starting several decades earlier and elastic subsidence due to long-term groundwater decline. While we do not have well data directly over those regions to perform a cross-correlation analysis between hydraulic head and ground deformation, we did observe that the spatial signature of those regions does not appear in the map of seasonal amplitude of ground deformation.

6.3. Aquifer and Fault Structure From InSAR Seasonal Deformation

The annual cycle of groundwater withdrawal and recharge, which was relatively constant from the early 1990s to 2008, resulted in regular ground deformation which oscillated in tandem with groundwater levels. In particular, we found that the short-term, annual ground oscillations were most correlated with fluctuations in hydraulic head in the principal aquifer system. The areas with the highest seasonal amplitudes in ground deformation were colocated with the areas of highest seasonal groundwater withdrawal. Additionally, we found that the amplitude of ground deformation was positively correlated with the total amount of groundwater withdrawal and head drawdown during the summer months.

Both the seasonal amplitude and phase maps suggest that within 10–15 km of the center of the basins, groundwater dynamics follow a standard diffusion process where hydraulic head changes propagate away from the zones of high withdrawal. Previous studies by OCWD that have approximated storage coefficients for the simplified three-layer model in the Santa Ana Coastal Basin show minimal variation in storage throughout the central regions of the basin, so the diffusion process should be relatively unperturbed there (Woodside & Westropp, 2015). However, we also observed sharp discontinuities in the seasonal phase due to the NIF and also within the basin away from any known fault systems (Figure 8). For the discontinuity within the basin, the seasonal phase changed from mid-March on the west side to late-April on the east side with an amplitude decrease of about 4 cm. From equation (6), we know that large spatial variations in ground deformation can be caused by large variations in hydraulic head, aquifer/aquitard thickness, or hydraulic diffusivity. We observed that the thickness of the principal aquifer system changed relatively rapidly in the location of the phase/amplitude discontinuity, which could mean that aquifer thickness controls the diffusion of hydraulic head throughout the aquifer system.

To investigate the effects of faults and aquifer thickness on observed ground displacement, we perform a series of simplified numerical experiments based on the diffusion equation for hydraulic head (equation (9)). We perform numerical simulations for three different scenarios: (1) constant hydraulic conductivity and aquifer thickness; (2) constant hydraulic conductivity and a step decrease in aquifer thickness; and (3) a narrow zone of low hydraulic conductivity and constant aquifer thickness. The last scenario is representative of head propagation across a narrow fault zone characterized by low permeability fault gouge. Note that for all three scenarios, S_s is fixed to be constant throughout the model domain so that any changes in diffusivity are controlled by changes in the conductivity. Equation (9) can be discretized using finite differences (central difference in space and forward difference in time) to obtain an explicit Euler update scheme to integrate the hydraulic head forward in time. We construct the x-domain to span from -40 to 40 km and choose a spatial resolution and time step in order to maintain solution stability. We place a sinusoidal source in the middle of the domain with a period of 1 year to simulate groundwater withdrawal and artificial recharge and set the head boundary conditions at the edges of the domain to be 0. We run the simulation for each scenario for several years and compute the amplitude and phase of the head response for each point in the domain.

The simulation results show that spatial discontinuities in the amplitude and phase of the hydraulic head are more likely due to a narrow zone of significantly different conductivity or aquifer thickness. Here our narrow zone of low hydraulic conductivity to emulate a fault produces results that best match our observations (Figure 19). Both the fault and rapid decrease in aquifer thickness cause an amplification of the amplitude of the head on the side closer to the source. However, the fault causes a step decrease in the amplitude (as observed in the InSAR results) while the thickness change maintains a continuous amplitude profile. Furthermore, only the fault causes a step increase in the phase. While we do not show the results
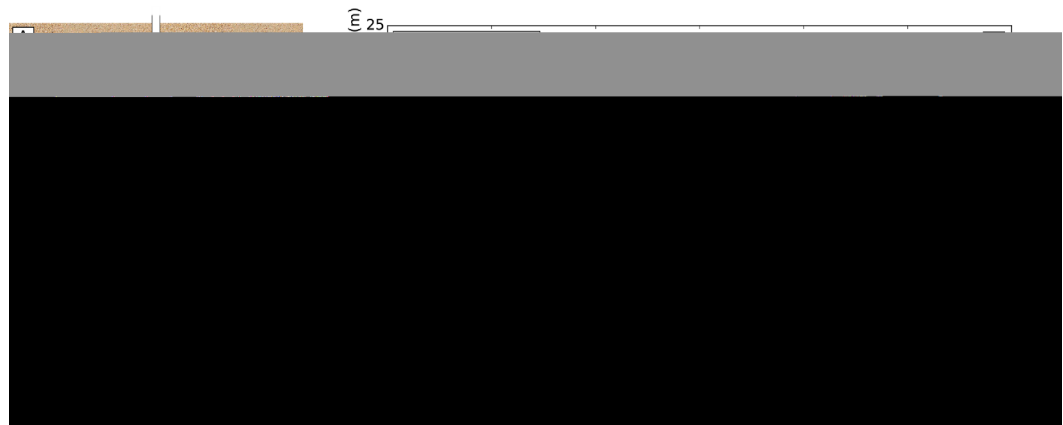
Figure 19. (a–c) Model setup for one-dimensional diffusion simulation with a periodic pressure source placed in the center of the domain. The three different models are (a) constant hydraulic conductivity and aquifer thickness, (b) constant hydraulic conductivity and a step decrease in aquifer thickness, and (c) narrow fault zone of low hydraulic conductivity and constant aquifer thickness. (f) The specific values for thickness and hydraulic conductivity for the three different scenarios. The amplitude and phase of the simulated hydraulic head in response to the periodic pressure source are shown in Figures 19d and 19e, respectively. The colors corresponding to the different models are (a) blue, (b) dashed blue, and (c) red. The sharp change in modeled head amplitude and phase for the fault simulation is most similar to the discontinuities observed in the InSAR results.

here, the same output could be obtained by modeling a narrow zone of very large aquifer thickness (i.e., a trench which is highly unlikely in a sedimentary basin) and a step decrease in hydraulic conductivity (see equation (9) to note the interchangeability between conductivity, K, and aquifer thickness, b). To represent the change from confined conditions to semiconfined or unconfined conditions in the margin of the basin, an equivalent formulation of a step decrease in hydraulic conductivity is a step increase in storage coefficient. The primary takeaway from these results is that in order to reproduce step changes in the amplitude and phase of the seasonal hydraulic head, it is necessary to have a rapid change of hydraulic conductivity confined to a *narrow* zone. This "fault" zone could very well be superimposed or adjacent to a step change in hydraulic conductivity since we do expect conductivity and specific yield to change in the forebay.

The nearest fault system is the Peralta Hills Fault (Figure 14), a reverse fault system located 10 km north of Santa Ana, California and about 5 km away from the observed discontinuity (Myers et al., 2003; Southern California Earthquake Data Center, 2012). The main fault is north-dipping with the last rupture possibly occurring in the Holocene, and its surface trace follows the curved boundary between the Santa Ana Coastal Basin and the adjacent Santa Ana Mountains. However, the extent of the fault system from the Peralta Hills into the alluvial plains is uncertain and not well mapped at depth. The discontinuity that we observe in our InSAR results could thus correspond to a blind branch of the Peralta Hills Fault with no observable surface trace. The discontinuity is also roughly coincident with the Anaheim Nose, an anticline with a north-west strike parallel to the Peralta Hills Fault (Bjorklund, 2003). However, the anticline is a broad feature with a crest between 1,500 and 3,000 m below the ground surface. Therefore, it is unlikely to affect groundwater flow in any observable manner.

One scenario we did not attempt to simulate is the difference in the aquifer units involved in groundwater withdrawal between the center of the basin and the margins (section 3.2). The likelihood that older, deeper units are involved in groundwater production in the margins as compared to younger, shallower units in the center is contrary to the simplified, one-dimensional point source simulation we performed here. The sharp boundary in the peak seasonal time we observe in the InSAR results could be associated with a lateral terminus of the younger unit pumped in the center of the basin. The delay in timing on the eastern side of the boundary could then be simulated by a separate system where lower vertical hydraulic conductivity is the driver for the later peak times.

7. Conclusions

We investigated the spatiotemporal ground deformation of the Los Angeles Central and Santa Ana Coastal Basins using a combination of GPS and C-band InSAR time series. We introduced a new method for

decomposing both time series into long-term and short-term signals in a spatially consistent manner using a distributed algorithm designed to solve large scale, regularized least squares problems very efficiently. This particular data set provided a unique opportunity to apply the time series analysis method on data with both time-varying seasonal signals and subtle transients caused by complex geophysical processes. The resultant time series decomposition allowed us to isolate the short-term ground deformation caused by seasonal variations in hydraulic head due to groundwater production practices that emphasized withdrawal during the summer months. The 18 year timespan of the InSAR data and the improved time series analysis resulted in spatially continuous maps of seasonal amplitude and phase of ground deformation with improved spatial resolution over previous studies. In particular, we were able to detect fine-scale features in the seasonal deformation including spatially varying pore pressure diffusion effects and a barrier to head diffusion due to a potential unmapped fault. The reconstructed long-term signals revealed subsidence over a wide area within the basins, as well as a 2–3 year uplift signal starting in 2004–2005 caused by a period of decreased ground production due to greater water availability. By comparing the time series results with hydraulic head data provided by WRD and OCWD, we were able to determine that ground deformation within the basins can be almost completely explained as an elastic response to head variations caused by groundwater production practices. Furthermore, we found that head variations in different parts of the aquifer system were responsible for the different time scales of ground deformation. Groundwater production is heavily monitored by agencies such as WRD and OCWD through a vast collection of monitoring well data. However, our results, in combination with previous InSAR studies over groundwater basins, show that analysis of InSAR time series data can be a useful tool for assessing the sustainability of pumping practices, and the continuing availability of data from new InSAR missions can be exploited by the hydrology community to aid groundwater monitoring over this area.

References

Alley, W. M., Healy, R. W., LaBaugh, J. W., & Reilly, T. E. (2002). Flow and storage in groundwater systems. *Science*, *296*(5575), 1985–1990.

Amelung, F., Galloway, D. L., Bell, J. W., Zebker, H. A., & Laczniak, R. J. (1999). Sensing the ups and downs of Las Vegas: InSAR reveals structural control of land subsidence and aquifer-system deformation. *Geology*, *27*(6), 483–486.

Bawden, G. W., Thatcher, W., Stein, R. S., Hudnut, K. W., & Peltzer, G. (2001). Tectonic contraction across Los Angeles after removal of groundwater pumping effects. *Nature*, *412*(6849), 812–815.

Berardino, P., Fornaro, G., Lanari, R., & Sansosti, E. (2002). A new algorithm for surface deformation monitoring based on small baseline differential SAR interferograms. *IEEE Transactions on Geoscience and Remote Sensing*, *40*(11), 2375–2383.

Bjorklund, T. (2003). The Whittier Fault trend: Cross sections, structure maps, and well tops in the major oil producing area of the northeastern Los Angeles basin. *American Association of Petroleum Geologists*. Search and Discovery, Article 10038.

Buckley, S. M., Rosen, P. A., Hensley, S., & Tapley, B. D. (2003). Land subsidence in Houston, Texas, measured by radar interferometry and constrained by extensometers. *Journal of Geophysical Research*, *108*(B11), 2542. https://doi.org/10.1029/2002JB001848

Chaussard, E., Bürgmann, R., Shirzaei, M., Fielding, E., & Baker, B. (2014). Predictability of hydraulic head changes and characterization of aquifer-system and fault properties from InSAR-derived ground deformation. *Journal of Geophysical Research: Solid Earth*, *119*, 6572–6590. https://doi.org/10.1002/2014JB011266

Chen, J., Knight, R., Zebker, H. A., & Schreüder, W. A. (2016). Confined aquifer head measurements and storage properties in the San Luis Valley, Colorado, from spaceborne InSAR observations. *Water Resources Research*, *52*, 3623–3636. https://doi.org/10.1002/2015WR018466

Ehman, K. D., Edwards, B. D., & Ponti, D. (2014). *Sequence stratigraphic framework of Upper Pliocene to Holocene sediments of the Los Angeles Basin, California: Implications for aquifer architecture*. Tulsa, OK: Pacific Section, SEPM, Society for Sedimentary Geology.

Farr, T. G., Rosen, P. A., Caro, E., Crippen, R., Duren, R., Hensley, S., et al. (2007). The shuttle radar topography mission. *Reviews of Geophysics*, *45*, RG2004. https://doi.org/10.1029/2005RG000183

Fetter, C. W. (2000). *Applied hydrogeology*. Upper Saddle River, NJ: Prentice Hall.

Galloway, D. L., & Burbey, T. J. (2011). Review: Regional land subsidence accompanying groundwater extraction. *Hydrogeology Journal*, *19*(8), 1459–1486.

Galloway, D. L., & Hoffmann, J. (2007). The application of satellite differential SAR interferometry-derived ground displacements in hydrogeology. *Hydrogeology Journal*, *15*(1), 133–154.

Galloway, D. L., Hudnut, K. W., Ingebritsen, S., Phillips, S. P., Peltzer, G., Rogez, F., et al. (1998). Detection of aquifer system compaction and land subsidence using interferometric synthetic aperture radar, Antelope Valley, Mojave Desert, California. *Water Resources Research*, *34*(10), 2573–2585.

Guenther, R. B., & Lee, J. W. (1996). *Partial differential equations of mathematical physics and integral equations*. North Chelmsford, MA: Courier Corporation.

Hantush, M. S. (1962). Flow of ground water in sands of nonuniform thickness: 2. Approximate theory. *Journal of Geophysical Research*, *67*(2), 711–720. https://doi.org/10.1029/JZ067i002p00711

Hauksson, E., Göbel, T., Ampuero, J.-P., & Cochran, E. (2015). A century of oil-field operations and earthquakes in the greater Los Angeles Basin, Southern California. *The Leading Edge*, *34*(6), 650–656.

Heath, R. C. (1982). Basic groundwater hydrology (Water Supply Pap. 2220). Reston, VA: US Geological Survey.

Hetland, E., Musé, P., Simons, M., Lin, Y., Agram, P., & DiCaprio, C. (2012). Multiscale InSAR time series (MInTS) analysis of surface deformation. *Journal of Geophysical Research*, *117*, B02404. https://doi.org/10.1029/2011JB008731

Hoffmann, J., Galloway, D. L., & Zebker, H. A. (2003). Inverse modeling of interbed storage parameters using land subsidence observations, Antelope Valley, California. *Water Resources Research*, *39*(2), 1031. https://doi.org/10.1029/2001WR001252

Jacob, C. (1950). Flow of ground water. In *Engineering hydraulics* (pp. 321–386). New York, NY: John Wiley.

Jolivet, R., Agram, P. S., Lin, N. Y., Simons, M., Doin, M.-P., Peltzer, G., et al. (2014). Improving InSAR geodesy using Global Atmospheric Models. *Journal of Geophysical Research: Solid Earth*, *119*, 2324–2341. https://doi.org/10.1002/2013JB010588

Keranen, K. M., Weingarten, M., Abers, G. A., Bekins, B. A., & Ge, S. (2014). Sharp increase in central Oklahoma seismicity since 2008 induced by massive wastewater injection. *Science*, *345*(6195), 448–451.

King, N., D., Argus, J., Langbein, D., Agnew, G., Bawden, R., Dollar, Z., et al. (2007). Space geodetic observation of expansion of the San Gabriel Valley, California, aquifer system, during heavy rainfall in winter 2004–2005. *Journal of Geophysical Research*, *112*, B03409. https://doi.org/10.1029/2006JB004448

Lanari, R., Lundgren, P., Manzo, M., & Casu, F. (2004). Satellite radar interferometry time series analysis of surface deformation for Los Angeles, California. *Geophysical Research Letters*, *31*, L23613. https://doi.org/10.1029/2004GL021294

Massonnet, D., Holzer, T., & Vadon, H. (1997). Land subsidence caused by the East Mesa geothermal field, California, observed using SAR interferometry. *Geophysical Research Letters*, *24*(8), 901–904.

Middleton, G. V., & Wilcock, P. R. (1994). *Mechanics in the earth and environmental sciences*. Cambridge, UK: Cambridge University Press.

Miller, M. M., & Shirzaei, M. (2015). Spatiotemporal characterization of land subsidence and uplift in Phoenix using InSAR time series and wavelet transforms. *Journal of Geophysical Research: Solid Earth*, *120*, 5822–5842. https://doi.org/10.1002/2015JB012017

Myers, D. J., Nabelek, J. L., & Yeats, R. S. (2003). Dislocation modeling of blind thrusts in the eastern Los Angeles basin, California. *Journal of Geophysical Research*, *108*(B9), 2443. https://doi.org/10.1029/2002JB002150

Riel, B., Simons, M., Agram, P., & Zhan, Z. (2014). Detecting transient signals in geodetic time series using sparse estimation techniques. *Journal of Geophysical Research: Solid Earth*, *119*, 5140–5160. https://doi.org/10.1002/2014JB011077

Schmidt, D. A., & Bürgmann, R. (2003). Time-dependent land uplift and subsidence in the Santa Clara Valley, California, from a large interferometric synthetic aperture radar data set. *Journal of Geophysical Research*, *108*(B9), 2416. https://doi.org/10.1029/2002JB002267

Southern California Earthquake Data Center. (2012). *Historical earthquakes and significant faults in southern CA.*

Terzaghi, K. v. (1923). Die berechnung der durchlassigkeitsziffer des tones aus dem verlauf der hydrodynamischen spannungserscheinungen. *Sitzungsberichte der Akademie der Wissenschaften in Wien, Mathematisch-Naturwissenschaftliche Klasse, Abteilung IIa*, *132*, 125–138.

Thiros, S., Bexfield, L., Anning, D., & Huntington, J. (2010). *Conceptual understanding and groundwater quality of selected basin-fill aquifers in the Southwestern United States* (Prof. Pap. 1781). Reston, VA: US Geological Survey.

Todd, D. K., Mays, L. W. *et al.* (1980). *Groundwater hydrology*. New York, NY: John Wiley.

Valentine, D. W., Densmore, J. N., Galloway, D. L., & Amelung, F. (2001). *Use of InSAR to identify land-surface displacements caused by aquifer-system compaction in the Paso Robles area, San Luis Obispo County, California, March to August 1997* (Open File Rep. 00447). Reston, VA: US Geological Survey.

Watson, K. M., Bock, Y., & Sandwell, D. T. (2002). Satellite interferometric observations of displacements associated with seasonal groundwater in the Los Angeles basin. *Journal of Geophysical Research*, *107*(B4), 2074. https://doi.org/10.1029/2001JB000470

Wilson, A., & Gorelick, S. (1996). The effects of pulsed pumping on land subsidence in the Santa Clara Valley, California. *Journal of Hydrology*, *174*(3), 375–396.

Woodside, G., & Westropp, M. (2015). *Orange country water district groundwater management plan 2015 update* (Technical report). Fountain Valley, CA: Orange County Water District.

Zhang, L., Lu, Z., Ding, X., Jung, H-S., Feng, G., & Lee, C.-W. (2012). Mapping ground surface deformation using temporarily coherent point SAR interferometry: Application to Los Angeles Basin. *Remote Sensing of Environment*, *117*, 429–439.